Seafloor shaping in mesophotic reefs, role of internal waves and bottom currents (Southeastern Mediterranean Sea)

Preprint: This manuscript is a non-peer-reviewed preprint submitted to EarthArXiv.

This manuscript has been submitted for peer review to Sedimentology

Seafloor shaping in mesophotic reefs, role of internal waves and bottom currents (Southeastern Mediterranean Sea)

Or M. Bialik[1,2,3]*; Henriette Wilckens[2]*; Omri Gadol[4,5]; Aaron Micallef[6]; Christian Betzler[7]; Ole Johannes R. Sørensen[8]; Hagai Nativ[8]; Yizhaq Makovsky[2,5]

1. Institute of Geology and Palaeontology, University of Münster, Corrensstr. 24, 48149 Münster, Germany

2. Dr. Moses Strauss Department of Marine Geosciences, The Leon H. Charney School of Marine Sciences, University of Haifa, Carmel 31905, Israel.

3. Israel Oceanographic and Limnological Research, National Institute of Oceanography, 310800, Haifa, Israel

4. CERENA, Instituto Superior Técnico, Lisbon University, Av. Rovisco Pais, 1049-001 Lisbon, Portugal

5. Hatter Department of Marine Technologies, Charney School of Marine Sciences, University of Haifa, Mount Carmel, 31905 Haifa, Israel.

6. Monterey Bay Aquarium Research Institute, Moss Landing, USA

7. Institute of Geology, CEN, University of Hamburg, Bundesstrasse 55, Hamburg 20146, Germany.

8. Morris Kahn Marine Research Station, The Leon H. Charney School of Marine Sciences, University of Haifa, Haifa, Israel

*Corresponding author (obialik@uni-muenster.de, hwilcken@campus.haifa.ac.il)

ABSTRACT

Mesophotic reefs are located in low light conditions which, depending on the region, found in water depths greater than ~30 m. They are less affected by ocean warming than reefs found in shallower water depth and thus might become increasingly important for the sustainability of marine biodiversity. Here we explore the physical mechanisms controlling the sediment distribution around a coralligenous mesophotic reef. A detailed survey of the Bustan HaGalil Ridge offshore Israel (30 to 50 m water depth) was carried out using an autonomous underwater vehicle with an interferometric synthetic aperture sonar, a multibeam echo sounder, and a sub-bottom-profiler. The data were combined with surface sediment samples, underwater photography, oceanographic data (measured and modeled current velocity) and water column seismic reflection data. The mesophotic reefs are built as a series of

asymmetric ridges (higher slope on the northeast-facing flanks) with coarse-grained biogenic sand to gravel within the valleys between the ridges. Two types of sedimentary bedforms are identified on the sediment surface - north-south elongated linear bedforms; and intersecting smaller bedforms, forming chevron shapes. Additionally, at the western margin of the ridge, a moat-drift contourite system is identified. The oceanographic data and modeling indicate that the northward flowing regional along slope current is strong enough to transport sediment. This explains the contourites, the ridge asymmetry and the increased accumulation of sediment at the southwest-facing slope of the ridges. The elongated linear bedforms are interpreted to be ripples attributed to internal waves, which are imaged in the water column off the shelf at the same depth as the bedforms. The chevron bedforms are suggested to be created by the interference of the bottom current with internal waves. In conclusion, the geometries of the mesophotic reefs, and the distribution of the sediment around them are controlled by internal waves and bottom currents.

Keywords: Levant, Synthetic Aperture Sonar, Bedforms, Coralline Algae, Sediment transport

INTRODUCTION

Benthic communities in poor light conditions that are found in depths between ca. 30 m and 150 m are commonly referred to as “mesophotic” (Baker et al., 2016). Mesophotic is a general term that encapsulates the range where light availability is reduced past its inflection point (~20%) and declines at a slower rate. However, the available light conditions in different water depths vary regionally and temporarily because of changes in weather, dust storms, productivity, and oceanographic processes that affect particle suspension in the water column. The exact definition of the mesophotic zone is not universally agreed upon (Bradford & Chang, 1987; Brokovich et al., 2008; Mitchell et al., 2000). Reefs located in the mesophotic zone are often located below or on the pycnocline in waters significantly cooler and more nutrient-enriched compared to shallow reefs (Kahng et al., 2019; Richardson & Bendtsen, 2019). Mesophotic reefs might be important as a refugia from environmental stress, such as results from climate change and anthropogenic disturbances (Bongaerts et al., 2010; Martinez et al., 2021). Despite their importance, mesophotic reefs are understudied compared to shallower reefs, possibly because they are more difficult to reach (Eyal et al., 2021; Menza et al., 2007). Mesophotic reefs exhibit a different benthic community and composition than reefs in shallower waters (Kahng et al., 2014; Rocha et al., 2018), and can have a significant coralline algae constituent (Amado-Filho et al., 2016). This coralline component means that the sediment and framework (coralligenous) production in mesophotic carbonate factories should be a sort of C-Type factory (*sensu* Schlager, 2005), with significant local grain export.

The depth in which mesophotic reefs are located implies that the processes that distribute sediments at shallower water reefs, such as waves and tides, are not able to generate the same effects in these deeper environments. Instead, the seafloor morphology in mesophotic environments is affected by bottom currents, which range from slope parallel to slope perpendicular (Church et al., 1985; Silva & MacDonald, 2017; Valle-Levinson et al., 2020; Williams et al., 1984). Ocean bottom currents flowing along a slope commonly lead to an elongated depression with an associated drift also referred to as a moat-drift system (Miramontes et al., 2021; Wilckens et al., 2023)(Miramontes et al., 2021; Wilckens et al., 2023). However, how these currents shape and control the sediment and nutrient transport around the reefs and shape their sedimentary morphology is not clear to this date. For example, the genetics of communities along mesophotic belts exhibit variable patterns (Bongaerts et al., 2013; Studivan & Voss, 2018). This may partly be due to variable light conditions within the reef (Laverick et al., 2020). However, the interaction with these bottom currents can also modulate the nutrient and temperature state to a level that may result in population shifts between periods of different current regimes (James et al., 1999; James & Lukasik, 2010).

Following the initial experimental work of Cacchione (1970), it has been suggested that internal waves may play a significant role in modulating turbidity, nutrients, heat and sediment distribution in mesophotic settings (Cacchione & Drake, 1986; Kahru, 1983; Pomar et al., 2012; Wolanski & Delesalle, 1995) as well as influence the evolution of reefs (Leichter et al., 1998; Lesser et al., 2009; Pomar et al., 2017; Schmidt et al., 2016; Wang et al., 2007; Wyatt et al., 2020). Internal waves are oscillations that propagate along internal stratification boundaries in the ocean (Talley et al., 2011). These waves are mostly generated by tides, but can be induced by wind waves as well (Nagasawa et al., 2000; Polton et al., 2008). Similar to waves at the ocean surface, internal waves also break, transfer energy and change frequency as they approach the seafloor. Internal waves may also break when they encounter an elevated structure, such as a reef (Davis & Monismith, 2011a). These internal wave breaks are an important dissipation and mixing mechanism (Lamb, 2014). The interaction of internal waves of different frequencies with the seafloor can resuspend and redistribute sediment similarly to wind waves nearshore (Boegman & Ivey, 2009; Cheriton et al., 2014; Quaresma et al., 2007). In addition to turbulence, breaking internal waves can redistribute heat and nutrients, significantly impacting deeper shelf / upper slope benthic communities (Woodson, 2018). However, how these waves interact with the seafloor in the mesophotic environment is poorly understood, as is the nature and type of bedforms they form (van Haren, 2017). With increasing stratification of the ocean, because of a change in temperature (Li et al., 2020), internal waves might become increasingly important in shaping reefs as well. This is true despite the significance

of bedforms, which influence sediment roughness and can enhance sediment resuspension (Soulsby et al., 2012).

The nature of seafloor interaction with both bottom currents and internal waves in the mesophotic setting needs to be better understood for the present and future dynamics of these systems, as well as their sustainability. The aim of this study is to examine the role of bottom currents and internal waves in a mesophotic reef. Using multiple data sets from the Bustan HaGalil Ridge offshore northern Israel (southeastern Mediterranean) this work documents sediment distribution and bedforms within a mesophotic reef system, in order to infer on the underlying mechanisms governing them.

OCEANOGRAPHIC AND GEOLOGICAL SETTING

Sediment distribution along the southeastern margin of the Levant Basin is controlled by a geostrophic current flowing northward (Figure 1a), with a seasonally changing transport component generated in shallower (<15 m depth) water by wave action (Almagor et al., 2000). The Levant Basin hosts several water masses that show seasonal depth variability (Alhammoud et al., 2005; Sisma-Ventura et al., 2016). During summer, the upper portion of the water column comprises two water masses. The warm and saline Levant Surface Water (LSW) between water depths of 0 and ca. 60 m, and the cooler and less saline Modified Atlantic Water (MAW) between water depths of 10 – 150 m. During winter, these two layers become mixed (Figure 1c, d). These water masses are underlain by the Levantine Intermediate Water (LIW) at depths of ca. 150 – 350 m, which oscillates on an interannual scale (Ozer et al., 2017). Internal waves propagate at the density boundary between the water masses and interact with the seafloor where they create sediment waves (Reiche et al., 2018).

In the oligotrophic to ultra-oligotrophic Levant Basin the nutricline does not overlap with the thermocline, notably with respect to nitrite and phosphate content (Kress & Herut, 2001; Krom et al., 2005). Ongoing warming further increases the ecological stress in the upper water column (Ozer et al., 2017; Rilov, 2016; Sisma-Ventura et al., 2014). This low productivity leads to high light penetration, with the 1% photosynthetic available light depths in the pelagic and neritic domains being at ~109±20m (n=21) and ~60±20 m (n=11), respectively (Berman et al., 1984; Megard & Berman, 1989; Stambler, 2014). Although, this figure varies with the season and meteorological events, such as dust storms that affect the region. Furthermore, rapidly increasing sea surface temperatures result in ongoing processes of species shift and “Tropicalization” in the coastal area of the Eastern Mediterranean (Bianchi, Carlo & Morri, 2003; Grossowicz et al., 2020; Rilov & Galil, 2009).

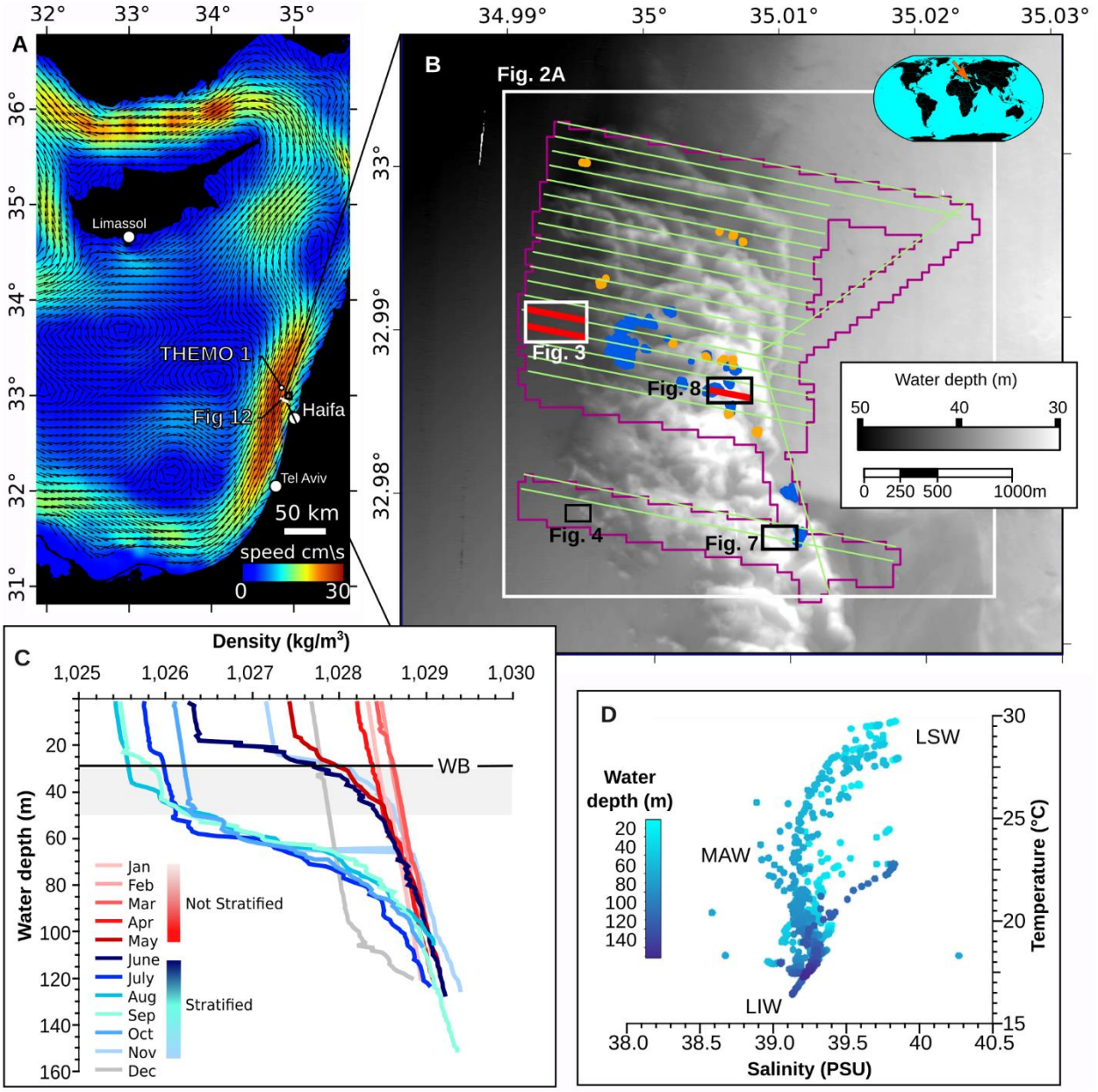

Figure 1: A. Modeled mean surface currents over 10 years (Global Ocean Physics Analysis and Forecast from the Copernicus network); Map of Israeli and southern Lebanese shelf showing the position of the study area and location of the THEMO 1 observatory buoy, inset shows the location of this map relative to the globe. B. Map of the study area, showing the overall bathymetry and location of Bustan HaGalil Ridge, areas of manual mapping of sediment bedforms and rocks (blue and orange, respectively) as well as the location of seismic lines (green), purple polygon delineates the outer parameter of the AUV survey. C. Annual variation in temperature at THEMO 1 in the top 150m (data from Reich et al., 2021), dark gray band outlines the annual amplitude of the pycnocline, light gry the depth distribution of sediment bedforms observed in this study, black line denotes the 99 percentile of effective wave depth which we consider as our wave base (WB). D. Salinity/temperature for the top 150 m at THEMO 1. MAW – modified Atlantic waters, LSW – Levant surface waters, LIW – Levant intermediate waters. e. Velocity data measured at THEMO 1.

The 10 to 20 km wide Southeastern Mediterranean Sea continental shelf comprises the eastern littoral cell of the Nile River, generally narrowing from south to north (Emery & Bentor, 1960). In general, the seafloor sediment grain size decreases significantly across the 30 m isobath, from fine sand to very fine sand with a significant clay and silt fraction (Almogi-Labin et al., 2012). However, in the northern part of the Israeli shelf (north of ca. 32.6°N), at the edge of the Nilotic littoral cell (the main source of siliciclastic grains in the region), the coarser grain fraction increases and extends past the 40 m isobath. This region is characterized by a higher carbonate content of up to 47% (Almogi-Labin et al., 2012), indicating a higher relative contribution of local sediment supply. Sets of generally shore parallel aeolianite ridges (locally referred to as Kurkar Ridges) stretch along the coastal zone and the middle shelf (~30 to 40 m water depth) of Israel (Almagor et al., 2000). These underlying aeolianite ridges have developed repeatedly in nearshore depositional environments, under the influence of the changing sea level during different Pleistocene glacial cycles (Mauz et al., 2013; Shtienberg et al., 2017). The offshore ridges form one of the main hard substrates on the shelf and serve as the base of most offshore reefs in the region (Rilov et al., 2018). These offshore reefs are presently being overwhelmed by invasive species (Peleg et al., 2020; Rilov, 2013). If similar to their presently coastal equivalents, the underlying aeolianites are composed of a mixture of biogenic grains (molluscan aragonite and coralline algae high-Mg calcite) and lithogenic quartz (Porat et al., 2003). These aeolianites are usually bound by two generations of cement - an early grain-coating micritic cement and a later pore-filling sparry cement.

Some of the most prominent aeolianite ridges are found in the shelf of northern Israel, including the study area of the Bustan HaGalil Ridge (Eytam & Ben-Avraham, 1992; Sade et al., 2006; Figure 1b). This is an elongated, up to 10 m tall, complex system of seafloor ridges. It extends for 7 km in the north-south direction and up to ~1.5 km in the east-west direction between water depths of 27 to 50 m. The Bustan HaGalil Ridge acts as a boundary between the soft (mostly silty) seafloor sediments to the west and mostly hard carbonaceous seafloor to the east.

MATERIALS AND METHODS

An ultra-high-resolution geophysical investigation of the seafloor environment of Bustan HaGalil Ridge (Figures 1b, 2) was carried out using the University of Haifa's ECA Robotics Inc. A18-UH deep-water surveying autonomous underwater vehicle (AUV) SNAPIR, operated off the Israel Oceanographic and Limnological Research Institute R/V Bat-Galim. The AUV survey was carried out on May 22, 2019, acquiring a total of 47 km hydroacoustic data over the northern half of Bustan HaGalil Ridge, at a flight elevation of 20 to 25 m above the seafloor in water depths of 25 to 50 m. Surveying involved data acquisition with: (1)

a 337 kHz Kraken Robotics MINSAS120 Interferometric Synthetic Aperture sonar (SAS), providing acoustic backscatter images with a swath width of 100 m to two sides and a resolution of 3 cm; (2) a Norbit WBMS 400 kHz multibeam echo sounder; (3) an Edgetech 2205 single channel Sub-Bottom Profiler (SBP) using a 2 to 10 KHz Chirp signal with a vertical resolution of ~20 cm.

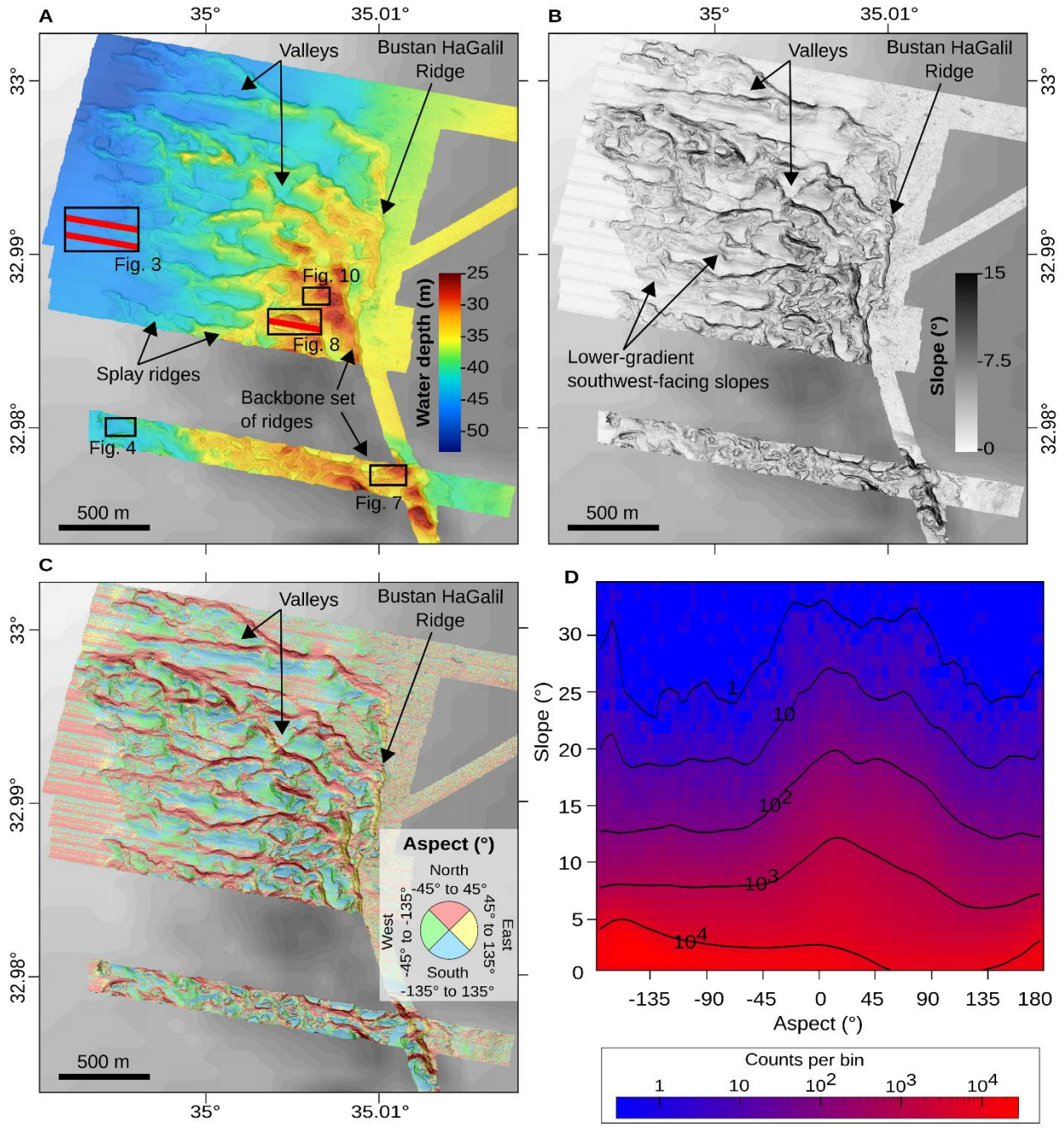

Figure 2: Bathymetric properties of the surveyed area: A. bathymetry; B. slope angle; C. aspect is divided in 4 colored sectors for north, east, south and west with a 65% transparency and underlighting slope map in Gray (as it is shown in B); D. density plot of the relations between aspect and slope, higher slopes occur with a NNE aspect while lower slopes have a more southern aspect. Binning for the density plot is 1° for slope and 5° for aspect. On top are contours in black.

The Sub-Bottom Profile (SBP) data were extracted as full-wave (Real) and were processed and interpreted using AspenTech SSE software suite. Following real time application of the matching filter, the post-processing scheme involved a minimum entropy deconvolution, 7.5 kHz high-cut filter and amplitude scaling. Multibeam data was processed with QPS Qimera (version 2.6.2) and resulted in a 1 m bathymetric grid. Spatial features were processed and analyzed in ESRI ArcGIS (Desktop version 10.8 and Pro) and QGIS (version 3.28). The multibeam bathymetry and SAS imagery were analyzed to identify the changes in seafloor characteristics across the study area. An analysis of the bedforms was performed across three selected soft sediment-rich areas of interest located in the western, central, and eastern part of the ridge; individual bedforms were manually traced and measured. Both starboard and port side imaging were compared (Supplement 1, Figure S1-1) to verify that there was no bias from the illumination direction. The survey was repeated with different illumination directions to compare the results and validate the measurements of the identified seafloor features. This is especially important for linear bedforms, such as ripples and sediment waves, as their appearance is dependent on the incidence angle (Supplement 1, Figure S1-2). In total, the crest length and orientation of 8324 bedforms and the widths of 5143 bedforms were measured (Supplement 2, for complete list). Visualization of statistical analysis was carried out using a combination of ArcGIS, MATLAB (MathWorks Inc., version 2022b), R software (R Core Team, 2024) with ggplot2 (Wickham, 2009) and QTIplot (Vasilief, 2010). In addition, 1053 rock features (small biogenic buildups, see discussion below) were identified, and their size and distribution were also measured. Sediment samples were collected via technical dives at selected locations, and visual documentation of seafloor features was used for ground truthing (Supplement 1, Figure S1-3). These sediment samples were washed with fresh water and air-dried prior to microscopy analysis. Mineralogical analysis was carried out using a Rigaku MiniFlex XRD diffractometer. Grain size was evaluated using the collected samples and by image analysis using ImageJ (of quadrats 25cm x 25cm) collected during the dive.

Wave and velocity data were obtained from the long-term THEMO1 buoy, located ~8 km northwest of the study area, and available from the THEMO project's website (http://themo.haifa.ac.il/) (Figure 1a). Details of the processing of the wave data (following Allen, 1985; Clifton & Dingler, 1984) and the raw data are given in the Supplementary Material (Supplement 3). Brunt–Väisälä frequency was calculated based on density data (Figure 1c) collected monthly in 2018 and 2019 next to the THEMO 1 buoy during research cruises described by Reich et al., (2021) and available through ISRAMAR (https://isramar.ocean.org.il/); values are included in cycles/hour and 10^{-2} rad 10^{-1} in Supplementary Material (Supplement 4). The data were processed and visualized using R Software and MATLAB. The multi-channel seismic profile showing data inside the water column (collected on 20.06.2016) was processed and interpreted using the SSE

(formally Paradigm) software suite. The processing procedure included high-pass filtration, amplitude balance, and time and time stack (using a moveout velocity of 1500 m/s). For converting Two Way Traveltime (TWT) into meters, a constant velocity of 1500 m/s was used. The Mercator Global Ocean Physics Analysis and Forecast model (1/12° resolution, from the copernicus network) was used to evaluate current velocities on a wider spatial coverage (https://doi.org/10.48670/moi-00016).

RESULTS

Ridges and sedimentary features of the Bustan HaGalil Region

Analysis of the bathymetry reveals that the Bustan HaGalil Ridge is composed of multiple ~1 to 1.5 km long generally east-west oriented rocky ridges that splay from a ~6 km long generally north-south oriented backbone set of rocky ridges. The ridge, in its entirety, dips to the west. High-resolution bathymetry of the northern part of the ridge shows that its eastern peaks reach water depths of ~25 mbpsl (meters below present sea level), ~10 m above the surrounding seafloor. Its western margins submerge into the mid-shelf sediment-covered seafloor that dip from a water depth of ~45 mbpsl in the ridge's southwestern edge to 50 mbpsl in its northwestern edge. The splay ridges are ~50-200 m wide (Figures 1b, 2; Supplement 1, Figure S1-4) with generally, elongated east-west trending valleys located between them (Figure 2d). The valleys are 100-500 m along their E-W axes and 50-100 m along their N-S axes. Some of the valleys are enclosed by the splay ridges while others are open on their western side (Figure 2a). The valley floors are shallowest in their eastern side at ~35 mbpsl and generally deepening ~45 mbpsl in the west.

The seafloor bathymetric gradients highlight the multi-scale variability of the seafloor morphology, with gradients of over 15° (<1% above 15°, some of which is suspected to be artifacts), with a mean gradient of 3.21°±3.10° (n=4,461,091), reflecting the hundreds-of-meters-scale dip of the entire ridge and its major elements (Figure 2d). At the tens-of-meter scale, the ridges are asymmetric, with wider lower-gradient southwest-facing slopes and narrower, steeper northeast-facing slopes (Figure 2a). At this scale, high gradients (>5°) are associated with aspects ranging between -30° and +60° (Figure 2d). The highest gradients at the meters scale appear at the northeast-facing slopes (Figure 2d). The northeast-facing slopes of the splay ridges terminate sharply (gradient >10°) at their bases (Figure 3). At this scale the topography of the northeast-facing slopes of the ridges appears smoother (Figure 3). Particularly in the southeastern part of the study area, the soft sediment in the valleys is bounded by a small 0.5-1 m tall step or very steep slope (~30°) (Figures 2b, 3a). The size of this step is smaller or disappears towards the northern side of the valley (Figures 2b, 3a). The seafloors between the splay ridges and part of the

southern side of the splay ridges are characterized by variable bedforms observed in the SAS data, to be discussed in detail in sections 'Bedforms of the Bustan HaGalil Region'.

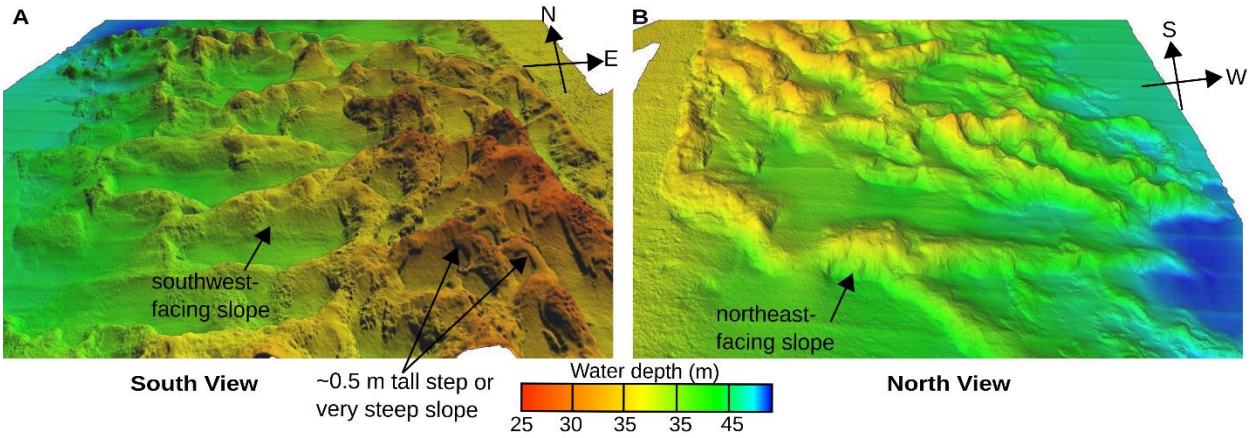

Figure 3: 3D shaded relief views (VE=8.5, light direction: altitude 45, Azimuth 45) of the Bustan HaGalil Ridge: A. from a south perspective and B. from a noth perspective, demonstrating the asymmetric nature of the features.

In the description below, we distinguish two types of mesophotic reef elements within the Bustan Hagalil Ridge. Continuous rocky elements with their long axis >10 m and a distinct relief are referred to as 'ridges/reefs'. Similarly, we define any continuous solid mass that its longer axis is ≤10 m and is spatially separate from any other rocky mass as a solitary reef/bioconstruction. This delineation is based on the observed dimensions of the non-continuous rock masses in the study area.

In SBP profiles, the Bustan HaGalil Ridge bedrock is characterized by high-amplitude, high-frequency, disrupted to chaotic reflections. In contrast, continuous, layered, medium amplitude to low amplitude reflections represent the sedimentary cover above the bedrock. The SBP data reveal that the main Bustan HaGalil Ridge bedrock structure is buried at its periphery by sub-meter-thick layered sediments, with their thickness increasing up to several meters outwards of the main bathymetric ridge (Figure 4). Some of the buried ridge peaks outcrop on the modern seafloor as solitary rocky elements. The bathymetric data show that northward-directed elongated depressions formed next to the western edges of the splay ridges (e.g., Figure 4a) and adjacent to the elongated depression are mounded morphologies. These are identified as moats with adjacent separated mounded drifts (Figure 4c). The SBP profiles show continuous seismic reflections extending from the moat to the drift, classifying it as a so-called constructional moat-drift system. The layered sediments exhibit onlap patterns (Figure 4b), at times leaning against the ridges at a slight angle. Evidence for scouring also appears in the SBP data, showing distorted and mounded layering in the vicinity of some of the ridges' promontories (Figure 4b, c). These appear in the uppermost (youngest) layers, as well as in some of the deeper (older) reflections imaged in the SBP.

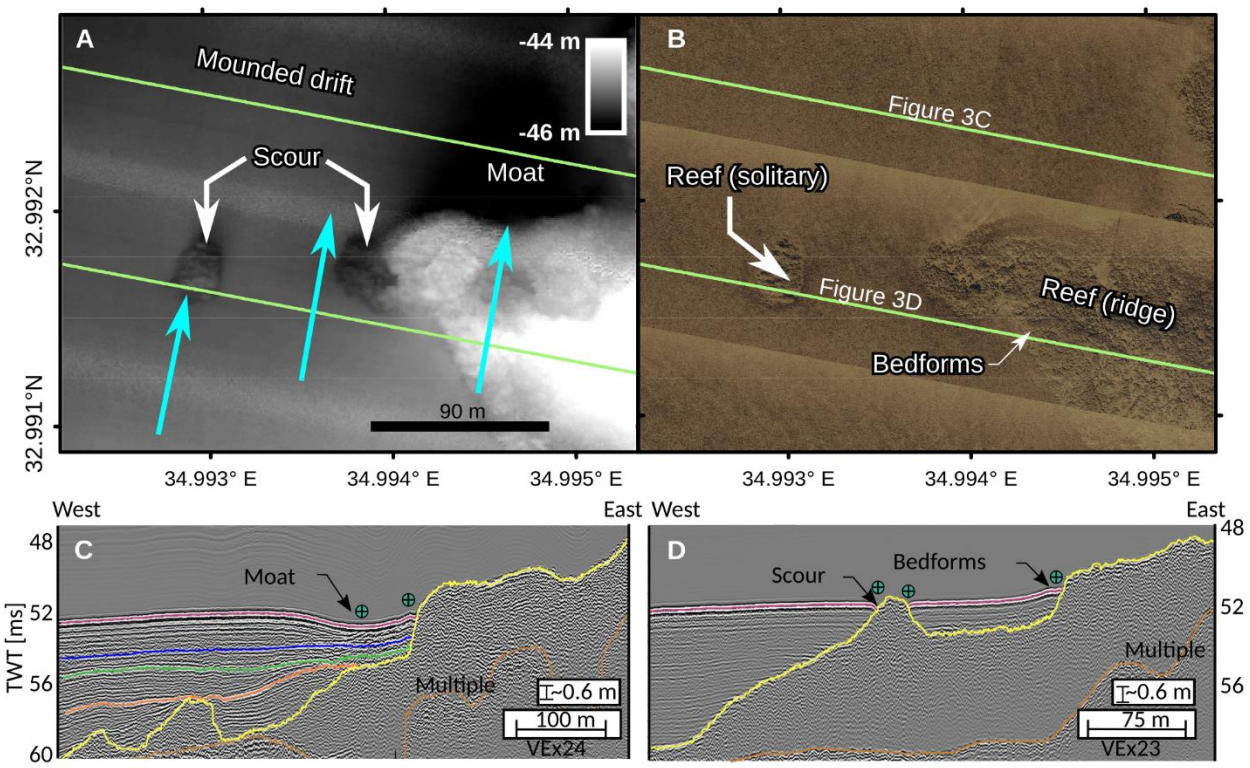

Figure 4: Character of the sediment on the western flank of the Bustan HaGalil Ridge. A. bathymetric and B. SAS image. Green lines show the location of the seismic lines, and blue arrows indicate the direction of the main current. C. interpreted seismic imaging showing the northern line. d. interpreted seismic imaging showing the southern line.

Bedforms of the Bustan HaGalil Region

SAS data reveal multiple bedforms inside the valleys. The types, sizes, and directions of bedforms change spatially within the valleys. Some bedforms are only visible with the SAS and cannot be distinguished at the resolution of the multibeam bathymetry (Supplement 1, Figure S1-5). Consequently, their relief is unknown. The SAS data shows that bedforms occur in three principal forms: large linear bedforms that look like ripples (Figure 5, 6d), short chevron bedforms that show a zigzag-like or v-shaped pattern (Figure 5, 6e), and superposition of the two (Figure 6f). Analysis of the manually traced bedforms (n=8325, Figure 1b) range in axis lengths from ~0.3 m to 70 m and wavelength from ~0.2 m up to 7 m, with the 10th to 90th percentile ranging between 0.6 and 1.9 m, respectively (Figure 7a). The linear bedforms are aligned primarily with a north-south bearing axis. Measurement of these bedforms reveals that these bedforms reach up to 70 m along their long axis (Figure 7b) and, for the most part, exhibit a maximum wavelength of up to 2 m. The chevron bedforms are shorter, with a northwest-southeast or northeast-southwest axis orientation (Figure 7c). Sometimes, chevron bedforms are observed superimposed on the linear bedforms (Figure 6f), whereas, in a few cases, they occur as poorly developed ladder-like bedforms (small bedforms linking adjacent larger ones) in between the linear bedforms.

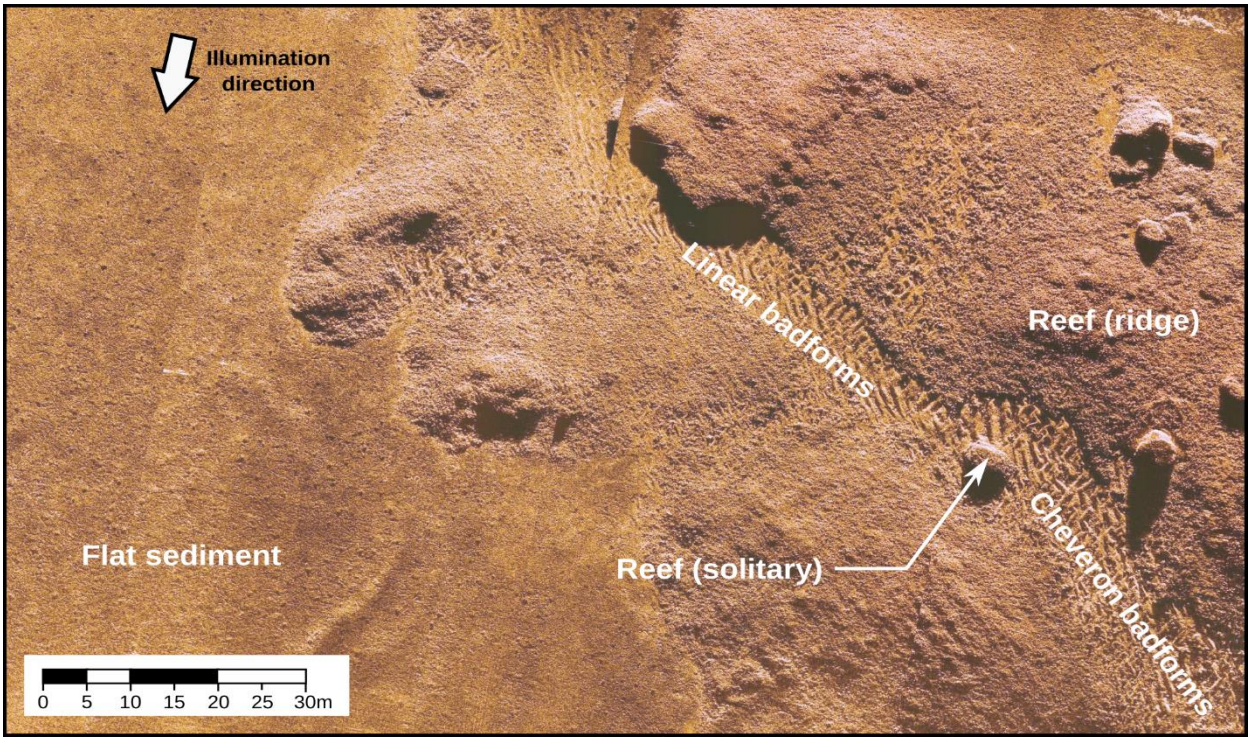

Figure 5: Wide-scope mosaic of the SAS imaging in the western margin of the survey area showing the three main seafloor types in the study area. See Figure 2 for location.

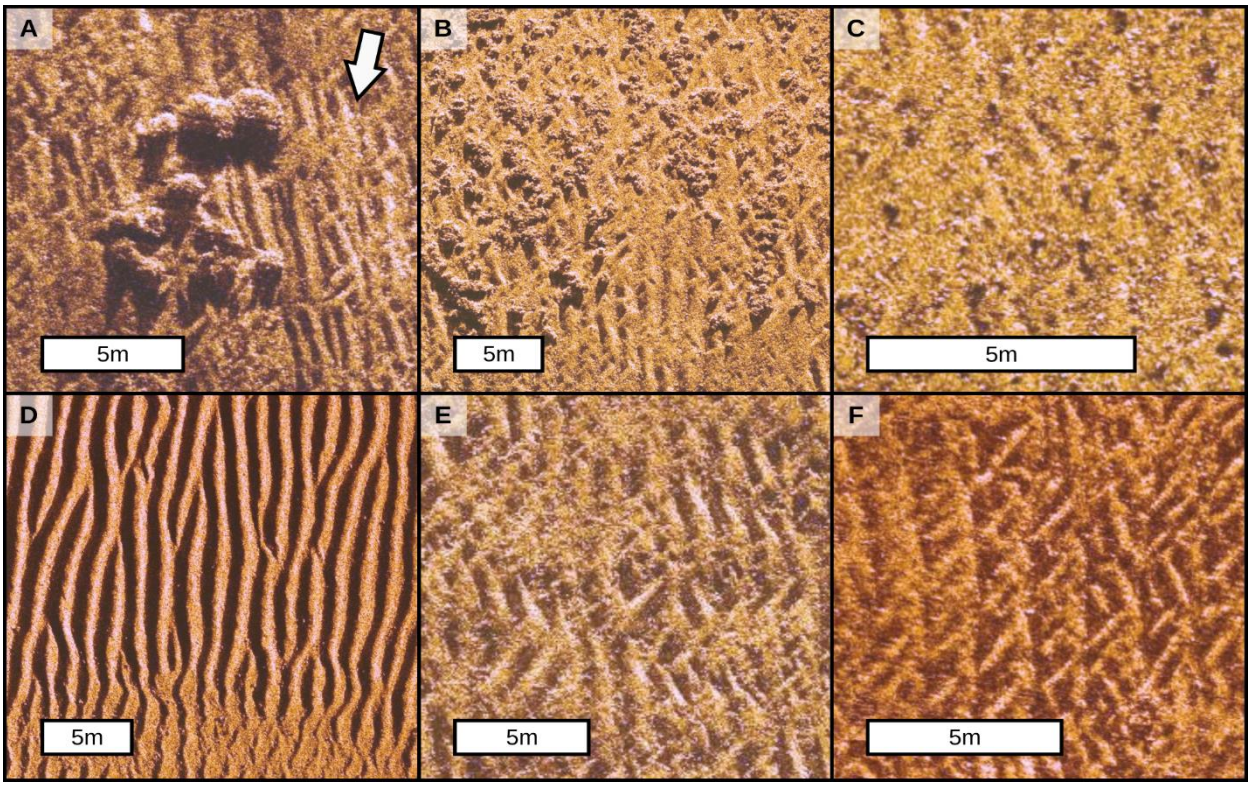

Figure 6: Representative SAS imaging of the seafloor features: A. large solitary bioconstruction (boulder size); B. intermediate constructions; C. small bioconstruction or rocks, suspected rhodolites; D. linear bedforms; E. chevron bedforms; F. superposition of chevron bedforms on top of linear bedforms. All scale bars are 5m, arrow in a shows illumination direction.

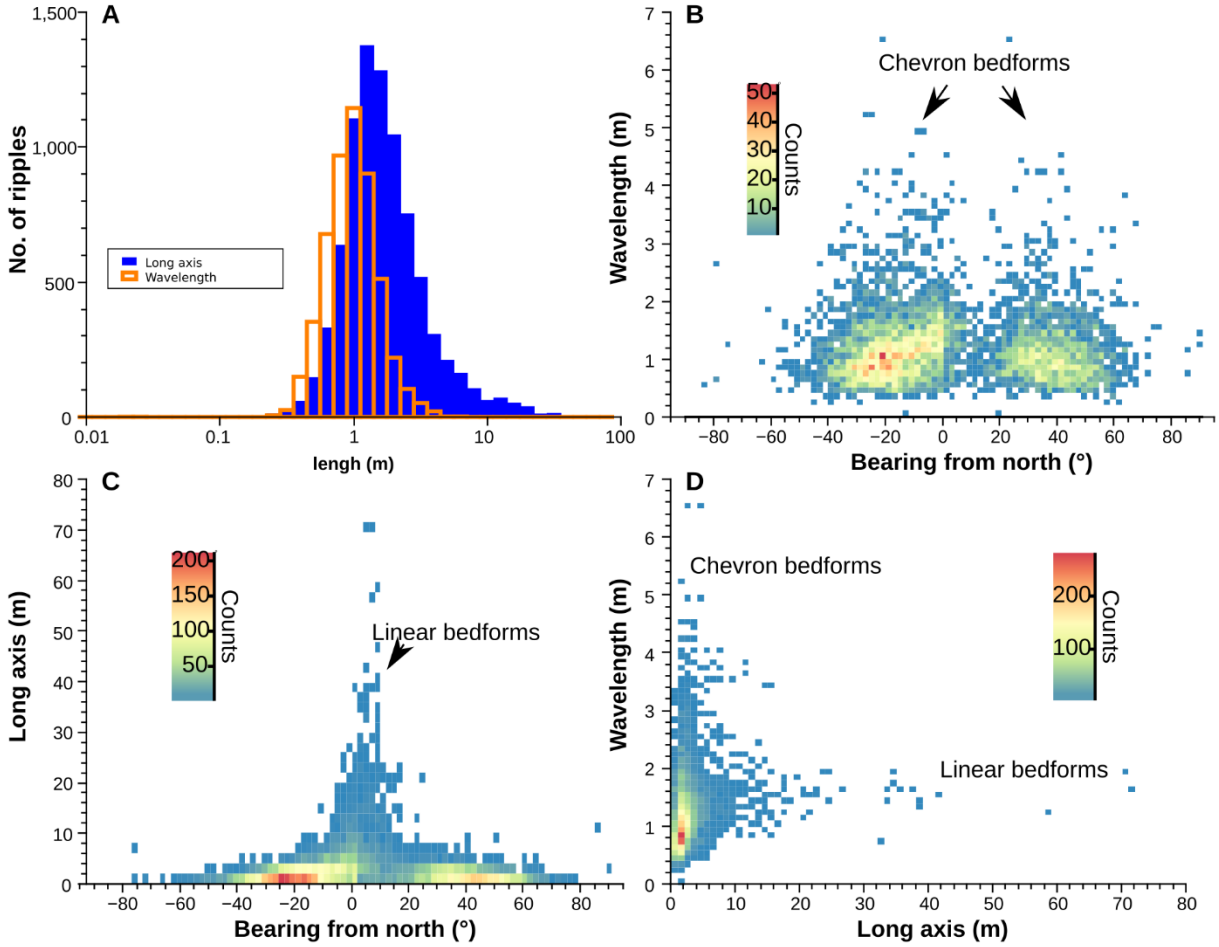

Figure 7: Bedform characteristics: A. distribution of long axis length (n=8323) and bedform wavelength (n=3557); B. relation between bearing and wavelength; C. relation between long axis length and bearing; D. relation between wavelength and long axis length.

Measurement of these bedforms reveals that the chevron bedforms extend to a maximum length of ~15 m and have a wavelength of up to 7 m. The bedforms are generally concentrated in stretches along the valleys and up the southward-facing slopes of the ridges (Figures 8, 9a). There seems to be a decrease in wavelength (from 2.5 m to 0.5 m) with increased seafloor slope or from the southern part of the valley to the north (Figure 8), but this was not observed consistently across the study area. The linear bedforms occur primarily in the southern margins of the valley, while the chevron bedform occurs primarily in the northern margin (Figure 9a). However, the chevron and mixed bedforms can also occur in the south of the valleys, but there they are very small (below 2 m along their long axis, and wavelength below 2 m). The SBP profiles reveal that transitions between chevron and linear bedforms coincide with an increase in sediment thickness (Figure 9b, c). The chevron bedforms are present where the sediment layer is

thinner, while the linear bedforms correspond to a thicker layer of sediment in the valleys. There is no clear correlation between the wavelengths and bedform axis lengths (r=≤0.19, n=5143; Figure 7d) nor either with the bearing (r=-0.01, n=5143 and r=0.01, n=8324, respectively). However, the relation between bedform wavelengths and bedform axis lengths shows two trends (with a gradient between them): a long axis / short wavelength cluster, which is mainly associated with linear bedforms, and a long wavelength / short axis cluster, which is mainly associated with chevron bedforms. There is no spatial trend concerning the wavelengths of the features, although there is a slight increase in axis lengths along the southwestern direction.

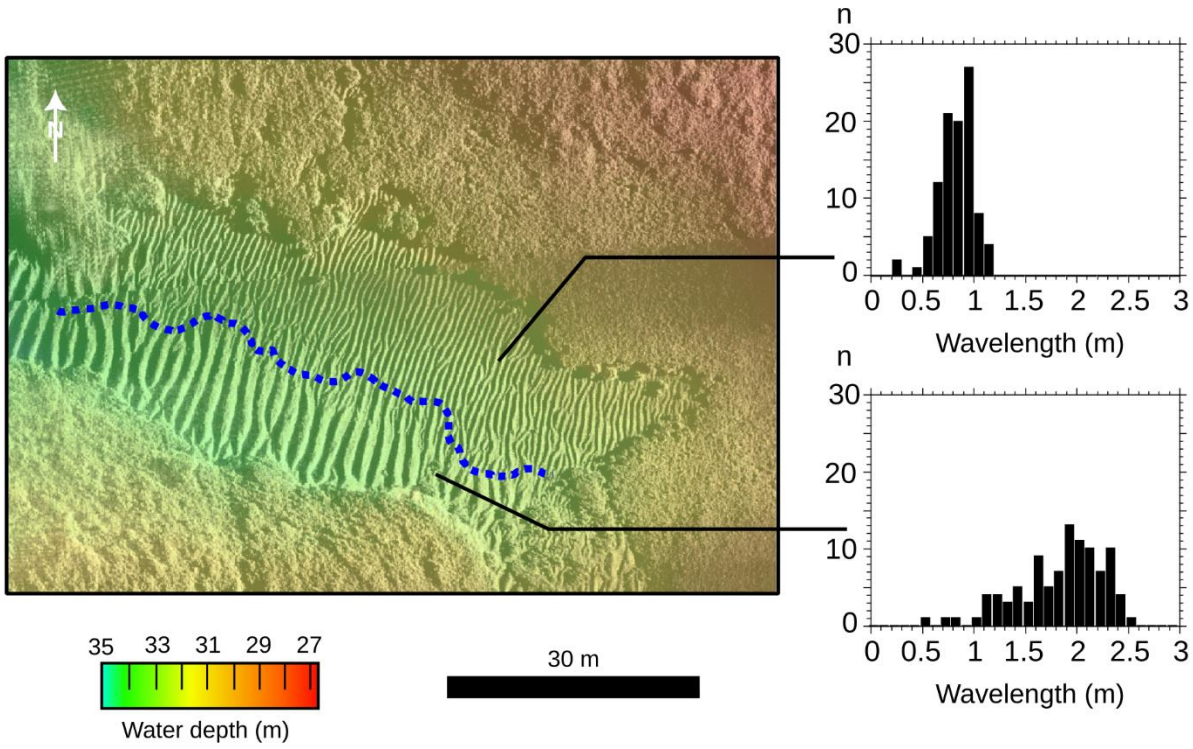

Figure 8: Relation between bathymetry and bedform morphology. Interlaced seafloor SAS seafloor image and bathymetry (note: slope is steeper south of the line), blue dashed line marks the transition between bedform morphologies. Histograms (n=100) show the change in wavelength on either side of the dashed blues line. See Figure 2 for location.

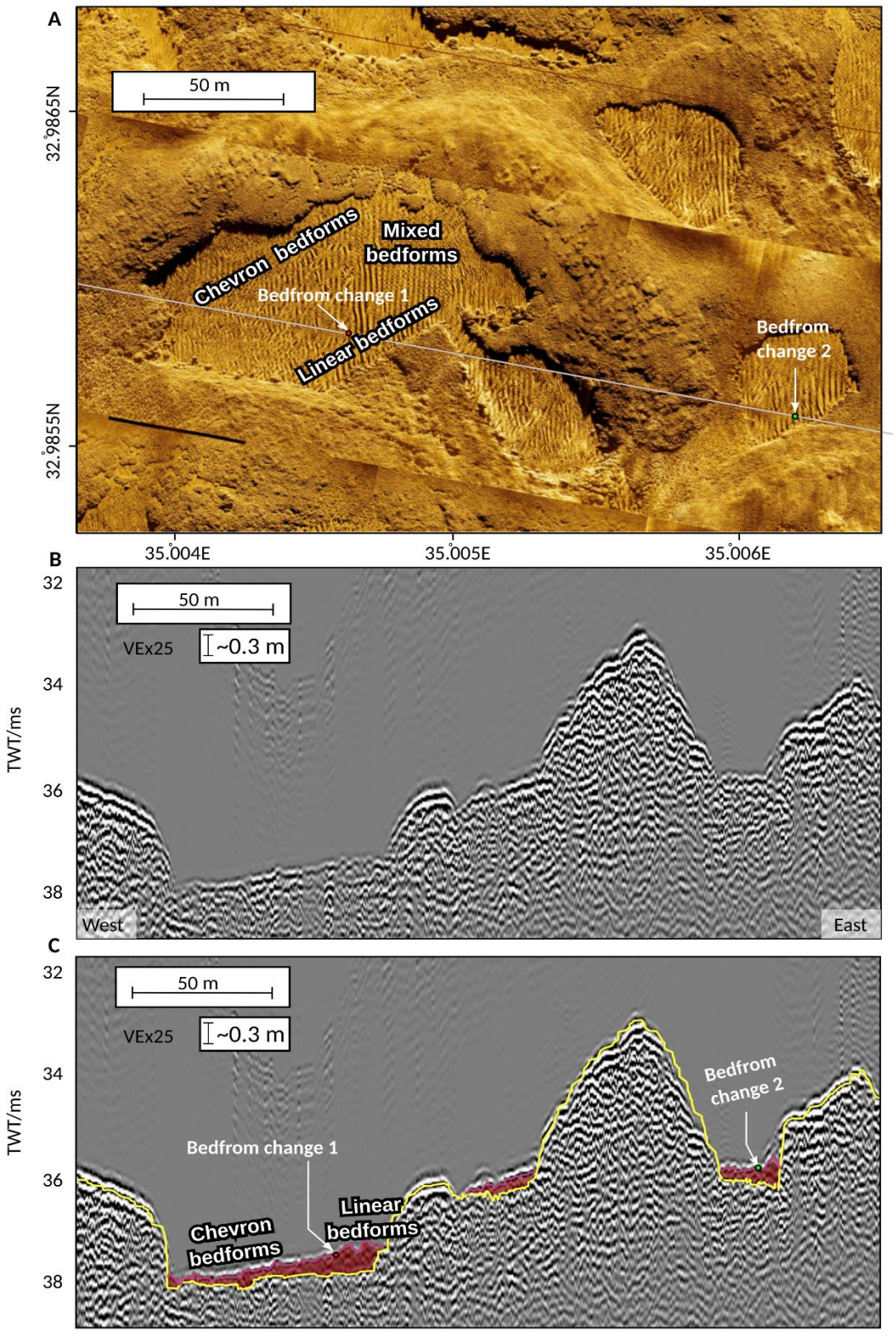

Figure 9: Seismic line across the sedimentary fill of the valleys, A. SAS imaging of the seafloor along the seismic line, the transition from chevron to linear bedforms marked. B. uninterpreted seismic imaging. C. interpreted seismic imaging showing the sedimentary fill (red) and the top of the rock surface (yellow). See Figure 2 for location.

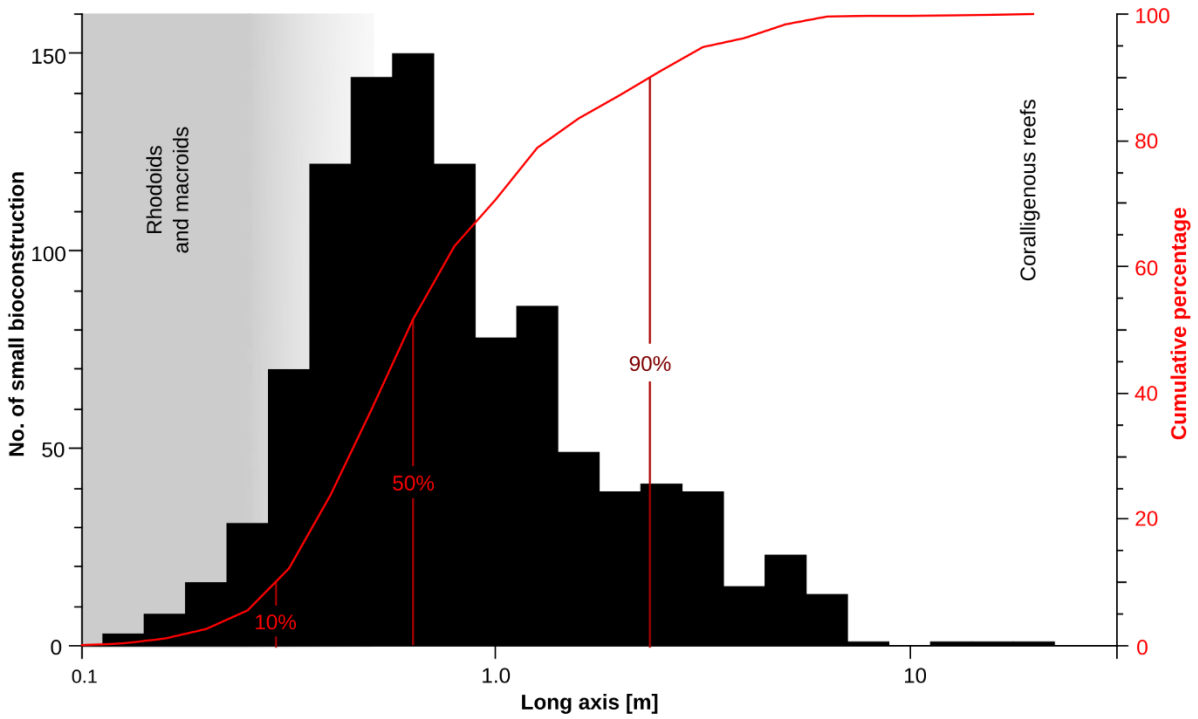

Figure 10: Long-axis size distribution (log scale) of rocks/bioconstructions sampled from the SAS imaging (n=1053), vertical lines denote the percentile fractions.

Solitary Reefs

Analysis of the bathymetry and SAS data reveals that the solitary reefs/bioconstructions occur in two main forms - adjacent to a ridge (Figure 5, 6a), or scattered between bedforms regardless of any ridge (Figure 6b, c), with the former often observed to be larger in size. The solitary reefs/bioconstructions vary from coarse gravel to boulders sizes (on the Wentworth, 1922 scale) and are observed to occur in the trough between bedforms or at the end point of bedforms. Adjacent to boulder size rocks/bioconstructions, a change in bedform character or direction is sometimes observed. The majority of rocky elements range from 0.13 m to 20 m along their long axis; the size distribution is highly skewed ($\tilde{\mu}_3$=5.2, n=1053; Figure 10) and > 50% of the rocky elements are under 0.76 m in length. Thus, around half of the rocky elements are classified as maerl (rhodoliths) and, as such, mobile (Hottinger, 1983). The larger rocks/bioconstructions and ridges/reefs show a crinkly texture, and in some places, individual branches (possibly of coralline algae or bryozoans) can be identified in the SAS images (Supplement 1, Figure S1-6), suggesting extensive biofouling of all available ha rd substrate.

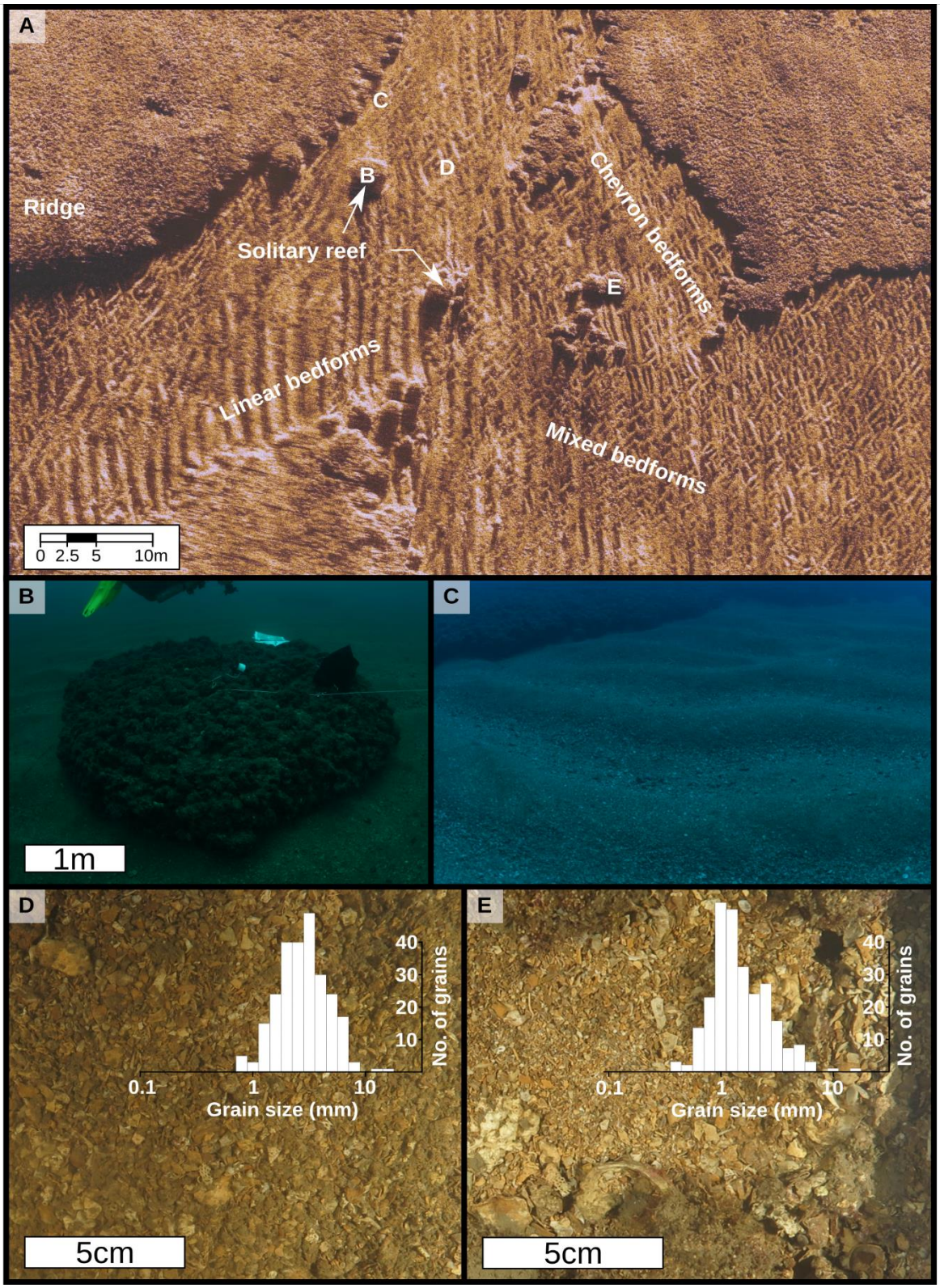

Figure 11: A. Configuration of bedform elements within a small valley, showing all types of bedforms and the location of subsequant subfigures. B. solitary reef/bioconstruction of encrusting organisms, notably coralline algae. C. individual bedforms at the base of the ridge. D. sediment and grain size distribution for the mixed bedforms. E. sediment and grain size distribution in the chevron bedforms. See Figure 2 for location.

Sedimentary Description

Visual inspection by divers examined both the rocks/ridges and ripple-like bedforms (Figure 11a). Over the rocks, they find an extensive biogenic cover (Figure 11b), which appears to comprise a meshwork of encrusting algae, foraminifera, and other organisms that can be classified as coralligenous (Supplement 1, Figure S1-3). Based on dive and analysis of the SAS data, the seafloor in the Bustan HaGalil Ridge region can be divided into three main substrate forms: reef/bioconstructions (reefs, rhodoliths, nodules etc.), ripple-like bedforms and a near-flat sediment surface. In contrast to the layered sediments around the Bustan HaGalil Ridge, the bedform patches within the Ridge's valleys, visible in SBP profiles, comprise a relatively thin sedimentary fill, overlying the bedrock (Figure 9). The maximum thickness of the sediment is ~0.6 ms (~0.5 m assuming a velocity of 1500 m/s).

The loose sediment samples collected by the divers comprise primarily calcareous grains ranging in sizes from coarse sand to coarse gravel (calcarenite to calcirudite *sensu* Grabau, 1904) with a major portion identified as fine to medium gravel (Figure 11c, d). The dive photographs of the bedforms area reveals that coarser grain sizes mainly occur in the troughs and finer grain sizes at the crests of the bedforms (Figure 11c). The grains are composed primarily of coralline algae nodules with other bioclastic fragments a few mm to cm in size (Figure 11d, e; Supplement 1, Figure S1-3). The nodules are brown, black or yellowish red, rounded, elongating or irregular in shape, ranging in size between a few mm and a few cm. Most of the coralline algae in the nodules appear to be dead, based on the color and presence of encrustation on some of the nodules. The encrustations are mainly formed by bryozoans, although serpulids or other vermiforms are observed as well as possibly some encrusting foraminifera (*Miniacina sp.* or *Homotrema sp.*). The bioclastic fragments include bivalves, gastropods, serpulids (or vermetid), echinoderms, and bryozoans; individual coral polyps were also found. Bryozoan fragments of multiple morphologies, including branching and encrusting forms, are common. A few larger benthic foraminifera are present, mainly the invasive species *Amphistegina sp.*

Local wind and surface wave character

The surface waves on the Galilee shelf, measured by the THEMO buoy, exhibit log-normal distributions of both the dominant period and significant wave height, with a log mean of 0.7±0.2 (4.8 m) and -0.3±0.3 (0.5 m), respectively (n=18841 for both). In contrast, the distribution of the mean period is closer to normal, with a mean of 3.7±0.7 s. Calculating the wavelength from the mean period (Figure 12, Supplement 5), results in a mean wavelength of 21.4±9.6 m (n=18686, 487 days across 2019 and 2020) and a $\tilde{\mu}_3$=1.8, the 10th percentile of 13.9 m, 90th percentile of 35.4 m, and a maximum wavelength of 84

m. This translates to a wave base shallower than 18 m for more than 90% of waves and only 1% reaching the depths of the sediment bedforms observed in the study area.

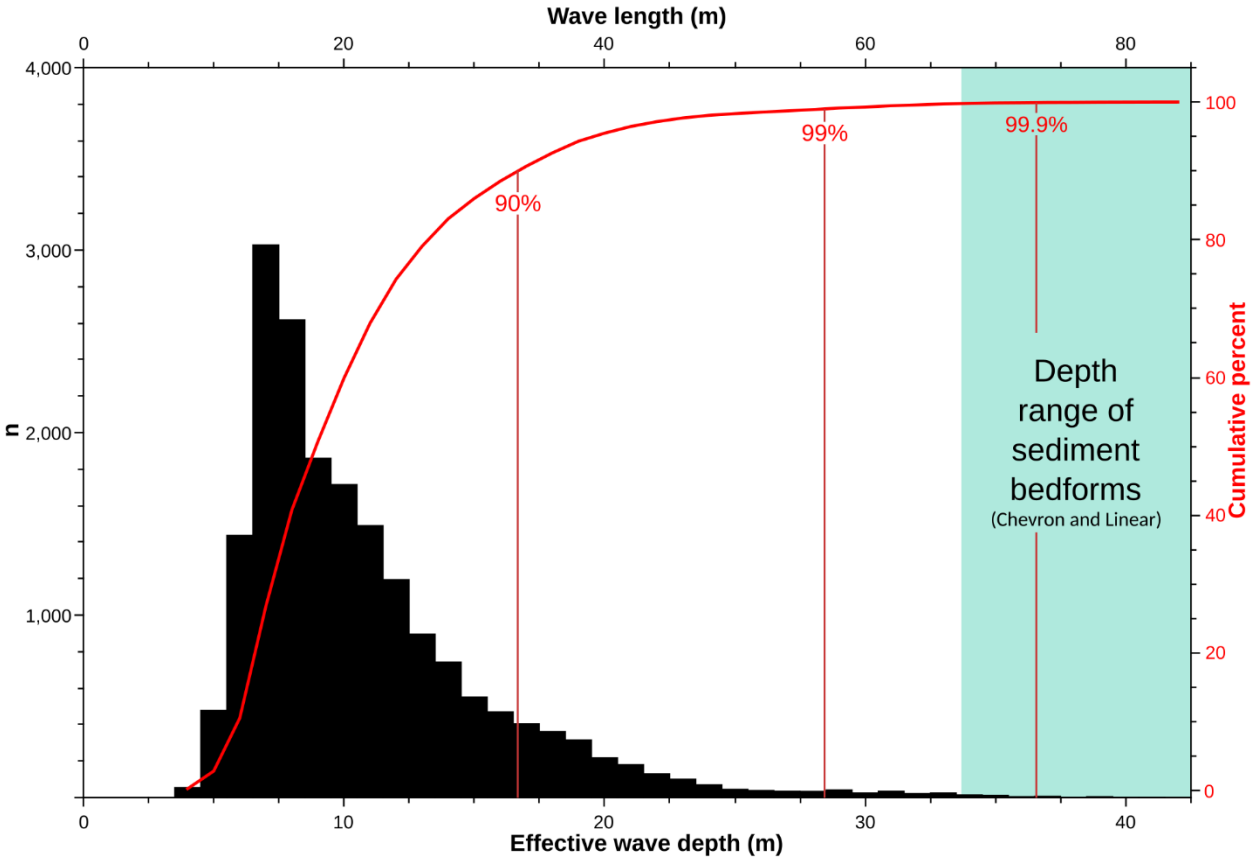

Figure 12: Wavelength distribution based on the THEMO 1 data, blue area marks the affected depth range in the study area.

Water column characteristics

The calculated Brunt–Väisälä frequency distribution exhibits low values (1.6±2.3 cycles/hour, $\tilde{\mu}_3$=1.2, n=563) during winter and spring months (December to April) (Figure 13). In the summer and autumn months (May to October), the values increase (5.9±5.5 cycles/hour, $\tilde{\mu}_3$=0.5, n=851). The highest frequencies (>25 cycles/hour) are located between 20 and 80 metres below present sea level (mbsl), with two main peaks (Figure 13) at 20 to 30 mbsl and 60 to 70 mbsl. High frequencies persist between these two peaks represent the migration of the pycnocline through the warm summer-autumn periods (Figure 1c). These values and distribution are comparable to previously published values for the southern Israeli shelf (Reiche et al., 2018). The high-resolution seismic sparker survey, acquired during the summer period (on 20.06.2016), imaged wavy, semi-continuous high-amplitude reflections at water depths between 30 and 50 mbsl (Figure 13). These wavy reflections appear similar to internal waves.

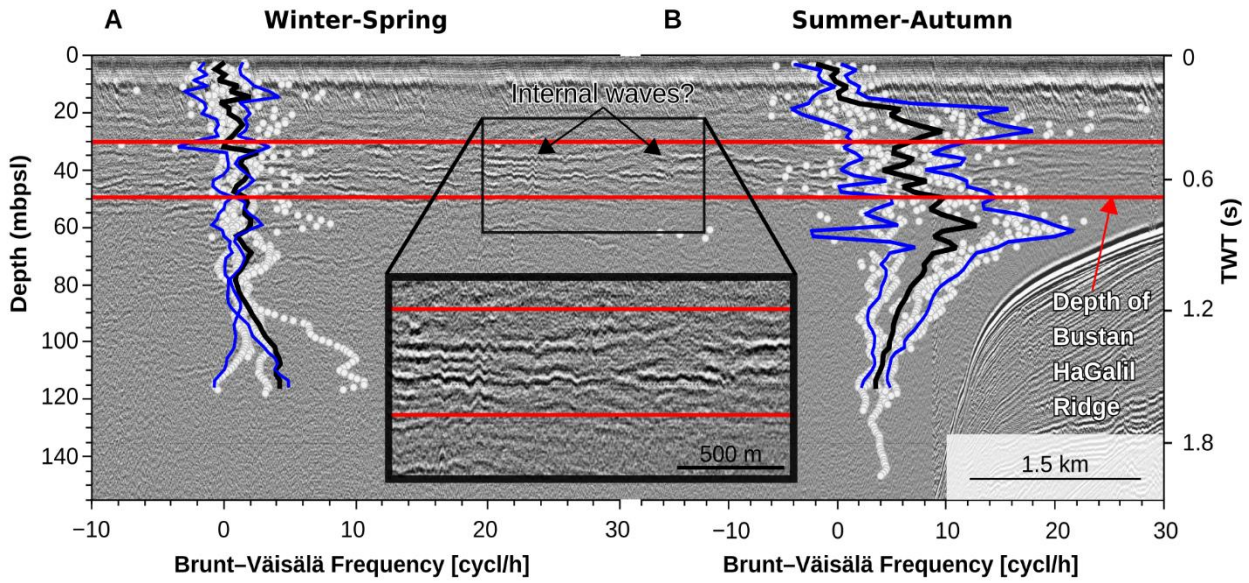

Figure 13: Distribution of Brunt–Väisälä frequencies in the water column during winter-spring and summer-autumn (see Figure 1C for density distribution over each month); black lines denote average and blue lines the 10% and 90% envalopes. The half-transparent background shows imaging of the water column with multi-channel seismics. This possibly shows internal waves between 30-50 m water depth, which is also the depth between the two peaks in the Brunt–Väisälä frequency.

Surface currents measured over 1 year at THEMO 1 have an average velocity of 21 cm/s with a standard deviation of 15 cm/s (Figure 14). Peak velocity is over 60 cm/s and the main current direction is north to north-east. Based on the Global Ocean Physics Analysis and Forecast from the Copernicus network modeled current averaged over 10 years it appears that the THEMO 1 buoy is located in the center of a main NNE flowing along-slope current, with the Bustan HaGalil Ridge also inside the same main current but more towards its eastern boundary.

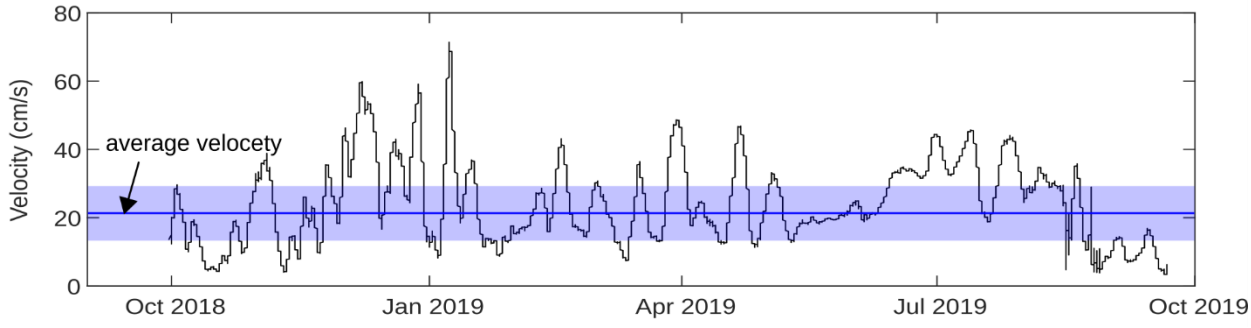

Figure 14: Near-surface current velocity measured at THEMO 1 over 1 year (average 21 cm/s with a standard deviation of 15 cm/s). See Figure 1a for location.

DISCUSSION

Biogenic structure

The Bustan HaGalil Ridge is a rocky structure in the middle of the northern Israeli shelf. The elevated parts of this structure offer hard substrates for the recruitment of various calcifying groups present in the Eastern Mediterranean. These include coralline algae, hydrozoans, bryozoans, sponges, larger benthic foraminifera, molluscs and potentially some corals (Albano et al., 2020; Cerrano et al., 2019; Corriero et al., 2019; Goren et al., 2021; Idan et al., 2018). Remains of many of these groups also occur in the sediment found in the submarine valleys of the Bustan HaGalil Ridge (Figure 11b-e). The binding, encrustation, and accumulation of these organisms results in the development of extensive coralligenous bioconstruction. Thus, the Bustan Hagalil Ridge is similar to other mesophotic reefs (also referred to as biogenic buildups) in the central Mediterranean Sea (Bialik et al., 2022; Ingrosso et al., 2018). The broad geometry of the Bustan Hagalil Ridge is similar to other Kurkar ridges in the coast and offshore of Israel. In the central Mediterranean, these are strongly influenced by the underlying Pleistocene strata (Varzi et al., 2023), as is likely the case here. However, the development of the biological cover and buildups is usually also controlled by local oceanographic conditions. Currents are most likely an important nutrient source that leads to differential biogenic growth rates on the south and north aspects of the ridges. Yet, with current data, one cannot constrain this with an evaluation of growth rates. Most Pleistocene beach ridges in the region are oriented north-south (Mauz et al., 2013) whereas the smaller splay ridges of Bustan Hagalil Ridge are oriented east-west (Figure 2d). This suggests that the modern structure evolved subaqueously through interactions of oceanography and biology.

The biogenic grains being mostly coralligenous, similar to the buildups, suggests that the fill of the sedimentary patches between the ridge, originate from the proximate buildups. The production of most of these components probably occurs predominantly on the highs and is then transported to the lower areas by current and gravity. Based on the size distribution (Figure 10) of the smaller rocky elements found on the sediment patches, and the prior description of large rhodoliths in this region of the Israeli shelf (Dulin et al., 2020), they are identified here as rhodoliths (Figure 6c). In difference to the other fragments, some coralline algae nodules in the sediment appear to focus on ongoing growth. Coralline algae can also grow on mobile substrates, and as such, their fragmentation from the crust can also lead to their transformation into nodules as they circulate by currents and animals (Braga & Martín, 1988). The production of calcium carbonate is most likely local and limited due to high stress and low nutrient availability in the region (Krom et al., 2005; Ozer et al., 2017; Thingstad et al., 2005). The limited

production potential is most likely one of the reasons for the observed relatively thin fill of the available relief/valleys between the ridges (Figure 8c).

Another control of biogenic contribution is the bioerosion and resuspension by fish, particularly by invasive species. The rocky reefs of the region have experienced a large-scale invasion of Indo-Pacific biota from the Red Sea through the Suez Channel (Edelist et al., 2013), in the process called 'Leseppsian migration'. Species such as the rabbit fishes *Siganus rividae* and *S. luridus* have led to a paradigm shift in the benthic macroalgae community, thereby affecting the overall ecosystem (Rilov et al., 2018; Sala et al., 2011). These herbivores are less abundant when compared to their occurrence in shallower reefs, but they are still present in reefs up to 45 meters depths (https://haifauniversity.shinyapps.io/FishsurveyApp2/). Other abundant species in the region such as *Scarus ghobban* and *Parupeneus forsskali* contribute significantly to the bioerosion and resuspension, respectively, in their native regions of the Red Sea (Alwany et al., 2009; Yahel et al., 2002). Although little is known of their effect on the redistribution of biotic and abiotic components in the Mediterranean rocky reef setting, it is likely that their role as ecosystem engineers affects the sediment composition, particularly in the ridge-sediment boundary and sediment patches within the ridges.

Mesophotic reefs are usually not affected by fair-weather waves resuspension (Baker et al., 2016). Lateral transport is of greater importance in mesophotic settings than deposition from the water column (Sherman et al., 2016). This redistribution of material impacts the lateral and vertical physical growth of the reef as well as the ecosystem that inhabits it, as is often the case in shallow water reefs (Hernández et al., 2009; Storlazzi et al., 2004). Here specifically, even an expanding evaluation of wave population would only allow for less than 1% of surface waves to affect the sediment and reef (Figure 12). Yet, when accounting to the relatively large grain size (Figure 11d, e) and maximum wave hight (Supplument 5), most of these waves would not be able to agitate the sediments in the valleys (Flemming, 2024).

Regional along slope current

To understand the sediment dynamics in the study area (discussed in the next section) the regional along slope current dynamics and its potential to transport sediment has to be evaluated. For the analyses of the current dynamics, a combined approach of large-scale and long-term modeling and local measurements is used. The model indicates a generally northward flowing along slope current and the local measurements show average current speeds of 21 cm/s with peak velocities over 60 cm/s. To evaluate if this current is strong enough near the seafloor to transport sediment we calculated the bottom shear stress $\tau = \rho u_*^2$, with seawater density ρ and friction velocity u_* (Soulsby & Whitehouse, 1997). Since

the current velocity measurements are from the sea surface the friction velocity needs to be calculated using a logarithmic relation between the friction velocity and the variation of velocity with height, a von-Kármán constant equal to 0.4 and bottom roughness length equal to 0.0035 m (Soulsby & Whitehouse, 1997). To move the seafloor sediments, the calculated bottom shear stress needs to reach the critical shear stress of 0.03 N/m^2 to initiate motion of sediment grain sizes in the very coarse sand to fine gravel range (1 mm - 3 mm). This corresponds to a velocity of 50 cm/s - 100 cm/s measured at the sea surface. The THEMO-1 measurements show that such velocities are reached during pick current periods, probably representing storm events (Figure 14) indicating that sediment can be moved. However, the sediment grain size in the study area is very diverse and reaches coarse gravel size in some areas. This indicates that the regional along-slope current is able to move the sand and fine gravel but not the coarse gravel.

Sediment dynamics and bedform development

The observed asymmetry of the splay ridges suggests that sediments transported along the Israeli margin towards the north are blocked by the splay ridges (oriented west to east) (Figures 2, 3). The sediment piles up at the southwest-facing side of the ridges, meaning that the sediment distribution in the valleys is asymmetric, with more sediment accumulating in the northern part. This sediment transport in the valleys towards the north explains the lower gradient of the southwest-facing side of the splay ridges. Thus, the sediment located in the valleys is mainly transported as bedload, which makes it impossible to cross over the ridge, unlike suspended sediment in the water column. This observation agrees with the calculations of the current's potential to transport sediment. Furthermore, currents that are strong enough to resuspend sediment flowing next to a slope or an obstacle like a reef commonly lead to the formation of moats (Faugères et al., 1999; Miramontes et al., 2021; Nielsen et al., 2009; Paulat et al., 2019; Wilckens et al., 2023). This is in agreement with our observation of a moat and adjacent separate mounded drift next to the Bustan HaGalil Ridge (Figure 4). Furthermore, the observed concentration of larger grain sizes in the Bustan HaGalil Ridge is probably the product of winnowing of smaller grain sizes, which in other mesophotic systems appear to be related to currents (Bialik et al., 2024). In general, the northeast-facing side of the ridges appear more smooth. This can be related to smaller grain sizes that can be affected by winnowing and are being deposited in the lee side of the ridges (meaning the northeast-facing side). Thus, the combined observations of a strong current flowing from south to north, a north south ridge asymmetry, the concentration of larger grain sizes and moat-drift systems next to the ridge all indicate that the regional along slope current is important for the sediment dynamics in the Bustan HaGalil Ridge.

The bedforms are located in the sediment patches in the valleys between the ridges and are large linear bedforms showing a wavy sediment structure (hereafter referred to as ripples, following Stow et al., 2009) and chevron bedforms that show a zigzag-like or v-shaped pattern. In general, ripples and sediment waves can be created by oceanic along slope currents, surface waves, and internal waves (Miramontes et al., 2021; Wynn & Stow, 2002).

To form ripples, the along slope current velocity has to be in a specific speed interval that depends on the sediment grain size according to the Bedford velocity matrix (Stow et al., 2009). As the previous discussion about the current dynamics in the study area has shown the currents are strong enough to move the sediment. However, ripples created by along slope currents are orthogonal to the current, while the north-south trends of the ripples align with the directions of the regional current observed over 10 years. The structure of the reef could influence the direction of the regional along slope bottom current, causing it to flow around the ridges. In the absence of current measurements close to the seafloor, it is impossible to examine this possibility. However, such a mechanism, if it occurs, would still fail to explain why the ripples are aligned north-south (Figure 7c) in areas that are enclosed by the reef structure (Figure 9). Thus, the regional along slope bottom currents cannot account for the formation of the ripples.

Without considering the size of the ripples, their morphology does look similar to ripples that form near the beach by surface waves. Since no more than 1% of the surface waves reach the depths of the sediment bedforms (Figure 12), it is unlikely that they could be the primary mechanism responsible for their formation. The fact that sediment is not consolidated and the badforms suggest continued agitation of the sediment to prevent cementation (Braithwaite et al., 2000). Yet the absence of common tracks or other indications or bioturbation suggests that this agitation is not biogenic and likely there is common repayment which erases such tracks.

An alternative to surface waves would be internal waves that can propagate on density boundaries inside of the water column (Talley et al., 2011). Features generated by internal waves elsewhere on the Israeli shelf exhibit wavelengths in the range of 10s to 100s of meters (Reiche et al., 2018), while the bedforms observed at Bustan HaGalil are at meters scale. Internal waves generated at shallower depths can be the product of resonance with the surface waves and thus have a higher frequency (Olbers & Eden, 2016). In this region, multiple domains and frequencies of internal waves are related to the local structure of the water column, notably the development of a strong pycnocline during summer (Figure 1c). This pycnocline is not depth-static but oscillates in depth and intensity throughout the year. It therefore may generate multiple energy states that interact with the seafloor. The Brunt–Väisälä frequency distribution calculated based on salinity and temperature data (Figure 13) indicates that internal waves can propagate in the

depth range in which the examined bedforms occur. This is especially the case during the summer-autumn period when the water body is more stratified. Internal waves have also been imaged with multi-channel seismic to the west of the study area in the same depth range of the observed bedforms (Figure 13). Thus, internal waves are the most likely cause for the ripples. To the west of the ridge, where external currents are more powerful, the impact of the interval waves is reduced because strong currents diminish the impact of internal waves (Stastna & Lamb, 2008) and, as a consequence, lead to the formation of the moat-drift systems.

The zigzag-like or v-shaped pattern of the chevron bedforms and their location within the valleys (with preference to the northern side, Figure 11a) suggests a complex mechanism of formation. These features also occur superimposed on the ripples. This suggests that their formation mechanism is spatially and/or temporally varying. The superposition of the chevron bedforms on the ripples (Figures 6f, 12a) suggests that the ripples formed first, the mechanism (internal waves) controlling them waned, and the one generating the chevron bedforms initiates. Alternatively, a combination of both mechanisms could also be responsible for the formation of mixed bedforms. So far, bedforms in shallower environments have been attributed to interference patterns between surface waves and currents (Baas, 2021; Dumas et al., 2005). In particular, the so-called tile-shaped interference ripples and ladder back ripples have a similar morphology to the here documented chevron bedforms and superposition of chevron bedforms with the ripples. However, the difference between the cases is that the shallower bedforms occur on cm-scale instead of meters-scale bedforms found in the study area. Thus, a similar combination of bottom current and waves is suggested here, where, in our case, the waves are internal waves rather than surface waves. The confines of the valleys and the multiple obstacles in and around them could result in wave reflection and refraction, which are known to define sediment distribution around reefs (Mandlier & Kench, 2012). While the chevron bedforms show some variability in orientation they trend in two main directions (Figure 7b), which suggests that they represent interference patterns. Such interferences could occur either between different refracted waves or with the incoming waves and could modify the apparent frequency, amplitudes and directions of the internal waves (Badiey et al., 2011; Oba & Finette, 2002).

It appears that the chevron bedforms are present where the sediment layer is thinner while the ripples correspond to thicker layer of sediment in the valleys. Based on the SBP the maximum thickness of the sediment in the valleys is ~0.5 m. Divers in the area have reported the bedforms to have a relive in the decimeter scale (personal communication). Possibly, a thin layer of sediment provides not enough material for the sediment ripples to grow as high as in areas with thicker sediment layer, which makes

them less stable. Consequently, the along slope bottom current could have a more visible effect on these ripples. Sediment ripples that get more sediment to grow with the energy provided by the internal waves might destroy the smaller influence from the along slope bottom current. This remains speculative because of the uncertainty of the sediment thickness and the bedford relief. Anyways, in a current controles setting there might also be a correlation between sediment grain size and sediment thickness. Wish can not be evaluated because of a lack of well distributed sediment samples. However, if such a correlation exists it could mean that the two types acutely depend on sediment grain size and not the sediment thickness. That bedforms in principle depend on grain size is well established (Stow et al., 2009). To evaluate this in the future more sediment samples are required or physical or numerical modeling is needed.

The ultra-high resolution of the SAS facilitates the identification of the bedforms, as these features would not have been well delineated by the bathymetry alone. Likely features of similar magnitude forming elsewhere have been missed due to limitations of the imaging technology. The findings from Bustan HaGalil Ridge support the argument that internal waves play an important role in modulating turbidity and sediment distribution in mesophotic settings (Pomar et al., 2012). However, they are not the only mechanism at play in this environment. The asymmetry of the ridges, the occurrence of chevron bedforms, and the moat-drift contourite systems indicate that regional bottom currents are also responsible for shaping the seafloor. Moreover, while coralline algae nodules require only slight agitation (Marrack, 1999), the distribution of the sediment grain sizes (Figure 11d, e) suggests the influence of significant transport energy. The existence of the mixed bedforms also indicates that the shaping mechanisms vary spatially. This interaction between regional bottom currents and internal waves most likely contributes also to shaping the coralligenous buildups. The mechanisms observed here are likely to also be present in open ocean mesophotic systems. In the Mascarene Plateau, for example, bottom currents and internal waves have been shown to be important agents of seafloor remodeling in mesophotic to shallow aphotic depths (Betzler et al., 2023; Bialik et al., 2024). However, while internal waves (Davis & Monismith, 2011b; Johnston & Colin, 2022; Marmorino, 2024; Wall et al., 2012) and bottom currents (Correa et al., 2012; Locker et al., 2016) have both been reported interacting with deeper reefs, there are few reports of both at play. This is possibly due to the different techniques usually used to detect either. To further understand the observed interference patterns and especially the temporal variability of the bedforms, repeated measurements in the same area are needed, together with mooring stations to measure internal waves and current velocity near the seafloor.

CONCLUSIONS

Mesophotic reefs represent a crucial but still underexplored marine niche. Sediment distribution in these settings are still very poorly understood. In this study, high-resolution acoustic imaging of a mesophotic reef system in the southeastern Mediterranean Sea was carried out. With cutting-edge imaging, it is possible to observe a mosaic of hard substrate reefs and maerl (rhodolith) beds interspersed with locally produced, coarse-grained, biogenic sediment. These sediments are redistributed by regional bottom currents and internal waves (Figure 15). The regional bottom current transports part of the sediment as bedload northward where it is blocked by the ridges/reef, leading to an asymmetry of the slopes. The large linear bedforms (here classified as ripples) are likely created by internal waves. The chevron bedforms are likely interference patterns created by the interaction between along-slope currents and internal waves. Similar bedforms might also occur in other mesophotic reefs but have previously not been studied in detail because of the absence of ultra-high resolution hydroacoustic imaging.

The full role of internal waves in mesophotic settings is still not fully understood. Implementation of high-resolution imaging with large spatial coverage (acoustic and/or photogrammetry) in other mesophotic settings is needed to improve our understanding of the dynamics in and around them.

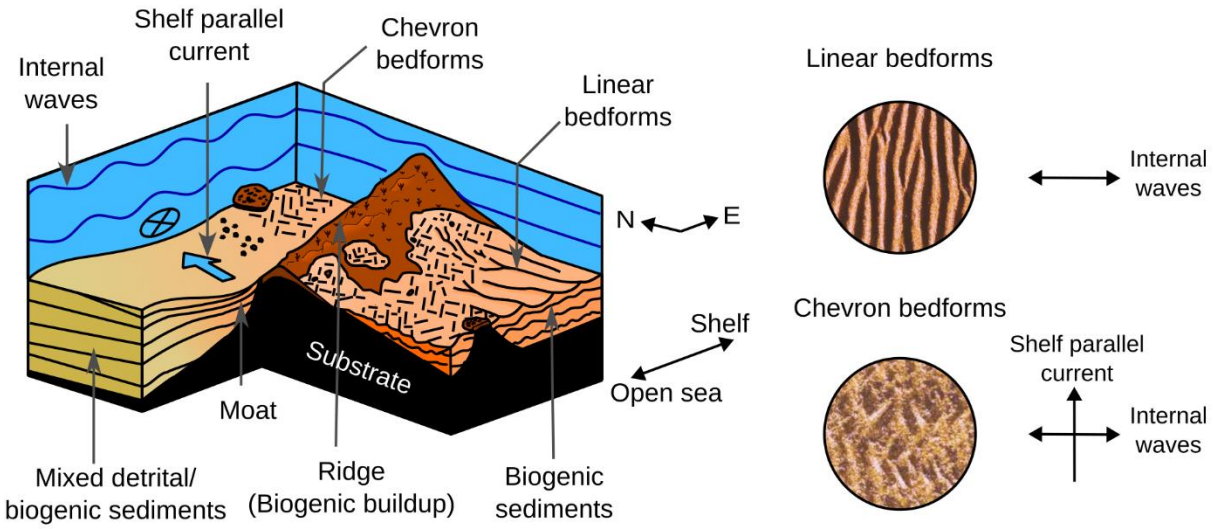

Figure 15: Schematic model (not to scale) of the bedform configuration and processes at play in the Bustan HaGalil Ridge.

ACKNOWLEDGEMENTS

OMB and HW are acknowledged as equal contributors. The data acquisition and initial analysis for this study were funded by the Israeli Nature and National Parks Protection Authority in collaboration with an anonymous donor to YM. Part of this study was conducted as part of OMB Marie Skłodowska Curie fellowship (101003394 — RhodoMalta). OMB and HOW are partially currently supported by the German (GEOMAR) - Israeli (University of Haifa) Helmholtz International Laboratory: The Eastern Mediterranean Sea Centre - An Early-Warning Model-System for our Future Oceans (EMS FORE). OG is currently supported by Marie Skłodowska Curie Fellowship 101180613 (GEM-SBP). AM was supported by the David and Lucile Packard Foundation. We thank Aspentech for contributing their SSE software suite; the AUV survey teams of the Hatter Department of Marine Technologies subsea vehicles lab. and S/V Shiqmona for collecting the geophysical data; and the technical diving teams of the Morris Kahn Marine Research Station and the Putsker Diving Center for the samples and visual data collection. The oceanographic buoy observatory data were kindly shared by the Texas A&M - University of Haifa - Eastern Mediterranean Observatory (THEMO) project. THEMO is operated by the Underwater Acoustic and Navigation Laboratory (ANL), Hatter Department of Marine Technology, University of Haifa, Israel, and by the Geochemical and Environmental Research Group (GERG), Texas A&M University, USA, and co-funded by the respective universities.

Data Availability

All supplementary and ancillary data sets are available via Figshare at https://figshare.com/s/6165f5654b4fb00183e7 (doi: 10.6084/m9.figshare.19642449). This study has been conducted using E.U. Copernicus Marine Service Information (https://doi.org/10.48670/moi-00016).

REFERENCES

Albano, P. G., Azzarone, M., Amati, B., Bogi, C., Sabelli, B., & Rilov, G. (2020). Low diversity or poorly explored? Mesophotic molluscs highlight undersampling in the Eastern Mediterranean. *Biodiversity and Conservation*, *29*(14), 4059–4072. https://doi.org/10.1007/s10531-020-02063-w

Alhammoud, B., Béranger, K., Mortier, L., Crépon, M., & Dekeyser, I. (2005). Surface circulation of the Levantine Basin: Comparison of model results with observations. *Progress in Oceanography*, *66*(2–4), 299–320. https://doi.org/10.1016/j.pocean.2004.07.015

Allen, J. R. L. (1985). *Principles of physical sedimentology*. Chapman and Hall.

https://doi.org/10.1007/978-94-010-9683-6

Almagor, G., Gill, D., & Perath, I. (2000). Marine Sand Resources Offshore Israel. *Marine Georesources & Geotechnology*, *18*(1), 1–42. https://doi.org/10.1080/10641190009353781

Almogi-Labin, A., Calvo, R., R., H. E., Amit, R., Harlavan, Y., Herut, B., & 1The. (2012). *Sediment Characterization of the Israeli Mediterranean Shelf (10-100 m)*.

Alwany, M. A., Thaler, E., & Stachowitsch, M. (2009). Parrotfish bioerosion on Egyptian Red Sea reefs. *Journal of Experimental Marine Biology and Ecology*, *371*(2), 170–176. https://doi.org/10.1016/j.jembe.2009.01.019

Amado-Filho, G. M., Moura, R. L., Bastos, A. C., Francini-Filho, R. B., Pereira-Filho, G. H., Bahia, R. G., Moraes, F. C., & Motta, F. S. (2016). Mesophotic ecosystems of the unique South Atlantic atoll are composed by rhodolith beds and scattered consolidated reefs. *Marine Biodiversity*, *46*(4), 933–936. https://doi.org/10.1007/s12526-015-0441-6

Baas, J. H. (2021). Current- and Wave-Generated Bedforms on Mixed Sand–Clay Intertidal Flats: A New Bedform Phase Diagram and Implications for Bed Roughness and Preservation Potential. *Frontiers in Earth Science*, *9*. https://doi.org/10.3389/feart.2021.747567

Badiey, M., Katsnelson, B. G., Lin, Y.-T., & Lynch, J. F. (2011). Acoustic multipath arrivals in the horizontal plane due to approaching nonlinear internal waves. *The Journal of the Acoustical Society of America*, *129*(4), EL141–EL147. https://doi.org/10.1121/1.3553374

Baker, E. K., Puglise, K. A., Colin, P., Harris, P. T., Kahng, S. E., Rooney, J. J., Sherman, C., Slattery, M., & Spalding, H. (2016). What are mesophotic coral ecosystems? In E. K. Baker, K. A. Puglise, & P. T. Harris (Eds.), *Mesophotic coral ecosystems—a lifeboat for coral reefs?* (pp. 11–19). The United Nations Environment Programme and GRID-Arendal.

Berman, T., Azov, Y., & Townsend, D. (1984). Understanding Oligotrophic Oceans : Can the Eastern Mediterranean be a Useful Model ? In O. Holm-Hansen, L. Bolis, & R. Gilles (Eds.), *Marine Phytoplankton and Productivity*. Lecture Notes on Coastal and Estuarine Studies, vol 8. Springer. https://doi.org/10.1007/978-3-662-02401-0_9

Betzler, C., Lindhorst, S., Reijmer, J. J. G., Braga, J. C., Lüdmann, T., Bialik, O. M., Reolid, J., Geßner, A., Hainbucher, D., & Bissessur, D. (2023). Carbonate platform drowning caught in the act: The

sedimentology of Saya de Malha Bank (Indian Ocean). *Sedimentology*, *70*(1), 78–99. https://doi.org/10.1111/sed.13032

Bialik, O. M., Betzler, C., Braga, J. C., Reijmer, J. J. G., Reolid, J., & Lindhorst, S. (2024). Changes in mesophotic carbonate-platform export across the end of the last glacial cycle (Saya de Malha Bank, western Indian Ocean). *The Depositional Record*. https://doi.org/10.1002/dep2.299

Bialik, O. M., Varzi, A. G., Durán, R., Le Bas, T., Gauci, A., Savini, A., & Micallef, A. (2022). Mesophotic Depth Biogenic Accumulations ("Biogenic Mounds") Offshore the Maltese Islands, Central Mediterranean Sea. *Frontiers in Marine Science*, *9*. https://doi.org/10.3389/fmars.2022.803687

Bianchi, Carlo, N., & Morri, C. (2003). Global sea warming and "tropicalization" of the Mediterranean Sea: biogeographic and ecological aspects. *Biogeographia – The Journal of Integrative Biogeography*, *24*. https://doi.org/10.21426/B6110129

Boegman, L., & Ivey, G. N. (2009). Flow separation and resuspension beneath shoaling nonlinear internal waves. *Journal of Geophysical Research: Oceans*, *114*(2), 1–15. https://doi.org/10.1029/2007JC004411

Bongaerts, P., Frade, P. R., Ogier, J. J., Hay, K. B., van Bleijswijk, J., Englebert, N., Vermeij, M. J., Bak, R. P., Visser, P. M., & Hoegh-Guldberg, O. (2013). Sharing the slope: depth partitioning of agariciid corals and associated Symbiodinium across shallow and mesophotic habitats (2-60 m) on a Caribbean reef. *BMC Evolutionary Biology*, *13*(1), 205. https://doi.org/10.1186/1471-2148-13-205

Bongaerts, P., Ridgway, T., Sampayo, E. M., & Hoegh-Guldberg, O. (2010). Assessing the 'deep reef refugia' hypothesis: focus on Caribbean reefs. *Coral Reefs*, *29*(2), 309–327. https://doi.org/10.1007/s00338-009-0581-x

Bradford, J. M., & Chang, F. H. (1987). Standing stocks and productivity of phytoplankton off Westland, New Zealand, February 1982. *New Zealand Journal of Marine and Freshwater Research*, *21*(1), 71–90. https://doi.org/10.1080/00288330.1987.9516202

Braga, J. C., & Martín, J. (1988). Neogene coralline-algal growth-forms and their palaeoenvironments in the Almanzora river valley (Almeria, S.E. Spain). *Palaeogeography, Palaeoclimatology, Palaeoecology*, *67*(3–4), 285–303. https://doi.org/10.1016/0031-0182(88)90157-5

Braithwaite, C. J. R., Taylor, J. D., & Glover, E. A. (2000). Marine Carbonate Cements, Biofilms,

Biomineralization, and Skeletogeneis: Some Bivalves Do It All. *Journal of Sedimentary Research*, *70*(5), 1129–1138. https://doi.org/10.1306/091699701129

Brokovich, E., Einbinder, S., Shashar, N., Kiflawi, M., & Kark, S. (2008). Descending to the twilight-zone: changes in coral reef fish assemblages along a depth gradient down to 65 m. *Marine Ecology Progress Series*, *371*, 253–262. https://doi.org/10.3354/meps07591

Cacchione, D. A. (1970). *Experimental study of internal gravity waves over a slope* [Massachusetts Institute of Technology and Woods Hole Oceanographic Institution]. https://doi.org/10.1575/1912/1348

Cacchione, D. A., & Drake, D. E. (1986). Nepheloid layers and internal waves over continental shelves and slopes. *Geo-Marine Letters*, *6*(3), 147–152. https://doi.org/10.1007/BF02238085

Cerrano, C., Bastari, A., Calcinai, B., Di Camillo, C., Pica, D., Puce, S., Valisano, L., & Torsani, F. (2019). Temperate mesophotic ecosystems: gaps and perspectives of an emerging conservation challenge for the Mediterranean Sea. *The European Zoological Journal*, *86*(1), 370–388. https://doi.org/10.1080/24750263.2019.1677790

Cheriton, O. M., McPhee-Shaw, E. E., Shaw, W. J., Stanton, T. P., Bellingham, J. G., & Storlazzi, C. D. (2014). Suspended particulate layers and internal waves over the southern Monterey Bay continental shelf: An important control on shelf mud belts? *Journal of Geophysical Research: Oceans*, *119*(1), 428–444. https://doi.org/10.1002/2013JC009360

Church, J. A., Andrews, J. C., & Boland, F. M. (1985). Tidal currents in the central Great Barrier Reef. *Continental Shelf Research*, *4*(5), 515–531. https://doi.org/10.1016/0278-4343(85)90008-1

Clifton, H. E., & Dingler, J. R. (1984). Wave-formed structures and paleoenvironmental reconstruction. *Marine Geology*, *60*(1–4), 165–198. https://doi.org/10.1016/0025-3227(84)90149-X

Correa, T. B. S., Eberli, G. P., Grasmueck, M., Reed, J. K., & Correa, A. M. S. (2012). Genesis and morphology of cold-water coral ridges in a unidirectional current regime. *Marine Geology*, *326–328*, 14–27. https://doi.org/10.1016/j.margeo.2012.06.008

Corriero, G., Pierri, C., Mercurio, M., Nonnis Marzano, C., Onen Tarantini, S., Gravina, M. F., Lisco, S., Moretti, M., De Giosa, F., Valenzano, E., Giangrande, A., Mastrodonato, M., Longo, C., & Cardone, F. (2019). A Mediterranean mesophotic coral reef built by non-symbiotic scleractinians. *Scientific*

Reports, *9*(1), 3601. https://doi.org/10.1038/s41598-019-40284-4

Davis, K. A., & Monismith, S. G. (2011a). The modification of bottom boundary layer turbulence and mixing by internal waves shoaling on a barrier reef. *Journal of Physical Oceanography*, *41*(11), 2223–2241. https://doi.org/10.1175/2011JPO4344.1

Davis, K. A., & Monismith, S. G. (2011b). The Modification of Bottom Boundary Layer Turbulence and Mixing by Internal Waves Shoaling on a Barrier Reef. *Journal of Physical Oceanography*, *41*(11), 2223–2241. https://doi.org/10.1175/2011JPO4344.1

Dulin, T., Avnaim-Katav, S., Sisma-Ventura, G., Bialik, O. M., & Angel, D. L. (2020). Rhodolith beds along the southeastern Mediterranean inner shelf: Implications for past depositional environments. *Journal of Marine Systems*, *201*, 103241. https://doi.org/10.1016/j.jmarsys.2019.103241

Dumas, S., Arnott, R. W. C., & Southard, J. B. (2005). Experiments on Oscillatory-Flow and Combined-Flow Bed Forms: Implications for Interpreting Parts of the Shallow-Marine Sedimentary Record. *Journal of Sedimentary Research*, *75*(3), 501–513. https://doi.org/10.2110/jsr.2005.039

Edelist, D., Rilov, G., Golani, D., Carlton, J. T., & Spanier, E. (2013). Restructuring the <scp>S</scp> ea: profound shifts in the world's most invaded marine ecosystem. *Diversity and Distributions*, *19*(1), 69–77. https://doi.org/10.1111/ddi.12002

Emery, K. O., & Bentor, Y. K. (1960). The continental shelf of Israel. In *Geological Survey of Israel Bulletin* (Vol. 26). State of Israel, Ministry of Development, Geological Survey.

Eyal, G., Laverick, J. H., Bongaerts, P., Levy, O., & Pandolfi, J. M. (2021). Mesophotic Coral Ecosystems of the Great Barrier Reef Are Understudied and Underexplored. *Frontiers in Marine Science*, *8*. https://doi.org/10.3389/fmars.2021.622856

Eytam, Y., & Ben-Avraham, Z. (1992). Morphology and sediments of the inner shelf off northern Israel. *Israel Journal of Earth-Sciences*, *41*(1), 27–44.

Faugères, J.-C., Stow, D. A. V., Imbert, P., & Viana, A. (1999). Seismic features diagnostic of contourite drifts. *Marine Geology*, *162*(1), 1–38. https://doi.org/10.1016/S0025-3227(99)00068-7

Flemming, B. W. (2024). The concept of wave base: fact and fiction. *Geo-Marine Letters*, *44*(3), 14. https://doi.org/10.1007/s00367-024-00776-3

Goren, L., Idan, T., Shefer, S., & Ilan, M. (2021). Macrofauna Inhabiting Massive Demosponges From

Shallow and Mesophotic Habitats Along the Israeli Mediterranean Coast. *Frontiers in Marine Science*, *7*, 612779. https://doi.org/10.3389/fmars.2020.612779

Grabau, A. W. (1904). *On the Classification of Sedimentary Rocks*. Wentworth Press.

Grossowicz, M., Bialik, O. M., Shemesh, E., Tchernov, D., Vonhof, H. B., & Sisma-Ventura, G. (2020). Ocean warming is the key filter for successful colonization of the migrant octocoral Melithaea erythraea (Ehrenberg, 1834) in the Eastern Mediterranean Sea. *PeerJ*, *8*, e9355. https://doi.org/10.7717/peerj.9355

Hernández, R., Sherman, C., Weil, E., & Yoshioka, P. (2009). Spatial and temporal patterns in reef sediment accumulation and composition, southwestern insular shelf of Puerto Rico. *Caribbean Journal of Science*, *45*(2–3), 138–150. https://doi.org/10.18475/cjos.v45i2.a3

Hottinger, L. (1983). Neritic Macroid Genesis, an Ecological Approach. In T. M. Peryt (Ed.), *Coated Grains* (pp. 38–55). Springer Berlin Heidelberg. https://doi.org/10.1007/978-3-642-68869-0_5

Idan, T., Shefer, S., Feldstein, T., Yahel, R., Huchon, D., & Ilan, M. (2018). Shedding light on an East-Mediterranean mesophotic sponge ground community and the regional sponge fauna. *Mediterranean Marine Science*, *19*(1), 84. https://doi.org/10.12681/mms.13853

Ingrosso, G., Abbiati, M., Badalamenti, F., Bavestrello, G., Belmonte, G., Cannas, R., Benedetti-Cecchi, L., Bertolino, M., Bevilacqua, S., Bianchi, C. N., Bo, M., Boscari, E., Cardone, F., Cattaneo-Vietti, R., Cau, A., Cerrano, C., Chemello, R., Chimienti, G., Congiu, L., … Boero, F. (2018). Mediterranean Bioconstructions Along the Italian Coast. *Advances in Marine Biology*, *78*, 61–136. https://doi.org/10.1016/bs.amb.2018.05.001

James, N. P., Collins, L. B., Bone, Y., & Hallock, P. (1999). Subtropical carbonates in a temperate realm; modern sediments on the Southwest Australian shelf. *Journal of Sedimentary Research*, *69*(6), 1297–1321. https://doi.org/10.2110/jsr.69.1297

James, N. P., & Lukasik, J. J. (2010). Cool- and cold-water neritic Carbonates. In N. P. James & R. W. Dalymple (Eds.), *Facies Models 4* (pp. 371–399). Geolocial Association of Canada.

Johnston, T. M. S., & Colin, P. L. (2022). Upwelling and Downwelling Driven by the North Equatorial Countercurrent and Internal Waves at Hatohobei Island and Helen Reef, Palau. *Journal of Geophysical Research: Oceans*, *127*(2). https://doi.org/10.1029/2021JC017606

Kahng, S. E., Akkaynak, D., Shlesinger, T., Hochberg, E. J., Wiedenmann, J., Tamir, R., & Tchernov, D. (2019). Light, Temperature, Photosynthesis, Heterotrophy, and the Lower Depth Limits of Mesophotic Coral Ecosystems. In Y. Loya, K. Puglise, & T. Bridge (Eds.), *Mesophotic Coral Ecosystems* (pp. 801–828). Coral Reefs of the World, vol 12. Springer. https://doi.org/10.1007/978-3-319-92735-0_42

Kahng, S. E., Copus, J., & Wagner, D. (2014). Recent advances in the ecology of mesophotic coral ecosystems (MCEs). *Current Opinion in Environmental Sustainability*, *7*, 72–81. https://doi.org/10.1016/j.cosust.2013.11.019

Kahru, M. (1983). Phytoplankton Patchiness Generated by Long Internal Waves: A Model. *Marine Ecology Progress Series*, *10*(2), 111–117.

Kress, N., & Herut, B. (2001). Spatial and seasonal evolution of dissolved oxygen and nutrients in the Southern Levantine Basin (Eastern Mediterranean Sea): chemical characterization of the water masses and inferences on the N:P ratios. *Deep Sea Research Part I: Oceanographic Research Papers*, *48*(11), 2347–2372. https://doi.org/10.1016/S0967-0637(01)00022-X

Krom, M. D., Woodward, E. M. S., Herut, B., Kress, N., Carbo, P., Mantoura, R. F. C., Spyres, G., Thingstad, T. F., Wassmann, P., Wexels-Riser, C., Kitidis, V., Law, C. S., & Zodiatis, G. (2005). Nutrient cycling in the south east Levantine basin of the eastern Mediterranean: Results from a phosphorus starved system. *Deep Sea Research Part II: Topical Studies in Oceanography*, *52*(22–23), 2879–2896. https://doi.org/10.1016/j.dsr2.2005.08.009

Lamb, K. G. (2014). Internal wave breaking and dissipation mechanisms on the continental slope/shelf. *Annual Review of Fluid Mechanics*, *46*, 231–254. https://doi.org/10.1146/annurev-fluid-011212-140701

Laverick, J. H., Tamir, R., Eyal, G., & Loya, Y. (2020). A generalized light-driven model of community transitions along coral reef depth gradients. *Global Ecology and Biogeography*, *29*(9), 1554–1564. https://doi.org/10.1111/geb.13140

Leichter, J. J., Shellenbarger, G., & Genovese, S. J. (1998). Breaking internal waves on a Florida (USA) coral reef: a plankton pump at work? . *Marine Ecology Progress Series*, *166*, 83–97. https://www.int-res.com/abstracts/meps/v166/p83-97/

Lesser, M. P., Slattery, M., & Leichter, J. J. (2009). Ecology of mesophotic coral reefs. *Journal of*

Experimental Marine Biology and Ecology, *375*(1–2), 1–8. https://doi.org/10.1016/j.jembe.2009.05.009

Li, G., Cheng, L., Zhu, J., Trenberth, K. E., Mann, M. E., & Abraham, J. P. (2020). Increasing ocean stratification over the past half-century. *Nature Climate Change*, *10*(12), 1116–1123. https://doi.org/10.1038/s41558-020-00918-2

Locker, S. D., Reed, J. K., Farrington, S., Harter, S., Hine, A. C., & Dunn, S. (2016). Geology and biology of the "Sticky Grounds", shelf-margin carbonate mounds, and mesophotic ecosystem in the eastern Gulf of Mexico. *Continental Shelf Research*, *125*, 71–87. https://doi.org/10.1016/j.csr.2016.06.015

Mandlier, P. G., & Kench, P. S. (2012). Analytical modelling of wave refraction and convergence on coral reef platforms: Implications for island formation and stability. *Geomorphology*, *159–160*, 84–92. https://doi.org/10.1016/j.geomorph.2012.03.007

Marmorino, G. (2024). A First Look at Internal Waves in the Great Barrier Reef Lagoon. *Remote Sensing*, *16*(12), 2180. https://doi.org/10.3390/rs16122180

Marrack, E. C. (1999). The Relationship between Water Motion and Living Rhodolith Beds in the Southwestern Gulf of California, Mexico. *PALAIOS*, *14*(2), 159. https://doi.org/10.2307/3515371

Martinez, S., Bellworthy, J., Ferrier-Pagès, C., & Mass, T. (2021). Selection of mesophotic habitats by Oculina patagonica in the Eastern Mediterranean Sea following global warming. *Scientific Reports*, *11*(1), 18134. https://doi.org/10.1038/s41598-021-97447-5

Mauz, B., Hijma, M. P., Amorosi, a., Porat, N., Galili, E., & Bloemendal, J. (2013). Aeolian beach ridges and their significance for climate and sea level: Concept and insight from the Levant coast (East Mediterranean). *Earth-Science Reviews*, *121*, 31–54. https://doi.org/10.1016/j.earscirev.2013.03.003

Megard, R. O., & Berman, T. (1989). Effects of algae on the Secchi transparency of the southeastern Mediterranean Sea. *Limnology and Oceanography*, *34*(8), 1640–1655. https://doi.org/10.4319/lo.1989.34.8.1640

Menza, C., Kendall, M., & Hile, S. (2007). The deeper we go the less we know. *Revista de Biología Tropical*, *56*. https://doi.org/10.15517/rbt.v56i0.5575

Miramontes, E., Thiéblemont, A., Babonneau, N., Penven, P., Raisson, F., Droz, L., Jorry, S. J., Fierens, R.,

Counts, J. W., Wilckens, H., Cattaneo, A., & Jouet, G. (2021). Contourite and mixed turbidite-contourite systems in the Mozambique Channel (SW Indian Ocean): Link between geometry, sediment characteristics and modelled bottom currents. *Marine Geology*, *437*, 106502. https://doi.org/10.1016/j.margeo.2021.106502

Mitchell, B. G., Bricaud, A., Carder, K., Cleveland, J., Ferrari, G., Gould, R., Kahru, M., Kishino, M., Maske, H., Moisan, T., Moore, L., Nelson, N., Phinney, D., Reynolds, R., Sosik, H., Stramski, D., Tassan, S., Trees, C., Weidemann, A., & Vodacek, A. (2000). Determination of spectral absorption coefficients of particles, dissolved material and phytoplankton for discrete water samples. *NASA Technical Memorandum*, 125–153.

Nagasawa, M., Niwa, Y., & Hibiya, T. (2000). Spatial and temporal distribution of the wind-induced internal wave energy available for deep water mixing in the North Pacific. *Journal of Geophysical Research: Oceans*, *105*(C6), 13933–13943. https://doi.org/10.1029/2000JC900019

Nielsen, S. G., Mar-Gerrison, S., Gannoun, A., LaRowe, D., Klemm, V., Halliday, A. N., Burton, K. W., & Hein, J. R. (2009). Thallium isotope evidence for a permanent increase in marine organic carbon export in the early Eocene. *Earth and Planetary Science Letters*, *278*(3–4), 297–307. https://doi.org/10.1016/j.epsl.2008.12.010

Oba, R., & Finette, S. (2002). Acoustic propagation through anisotropic internal wave fields: Transmission loss, cross-range coherence, and horizontal refraction. *The Journal of the Acoustical Society of America*, *111*(2), 769–784. https://doi.org/10.1121/1.1434943

Olbers, D., & Eden, C. (2016). Revisiting the Generation of Internal Waves by Resonant Interaction with Surface Waves. *Journal of Physical Oceanography*, *46*(8), 2335–2350. https://doi.org/10.1175/JPO-D-15-0064.1

Ozer, T., Gertman, I., Kress, N., Silverman, J., & Herut, B. (2017). Interannual thermohaline (1979–2014) and nutrient (2002–2014) dynamics in the Levantine surface and intermediate water masses, SE Mediterranean Sea. *Global and Planetary Change*, *151*, 60–67. https://doi.org/10.1016/j.gloplacha.2016.04.001

Paulat, M., Lüdmann, T., Betzler, C., & Eberli, G. P. (2019). Neogene palaeoceanographic changes recorded in a carbonate contourite drift (Santaren Channel, Bahamas). *Sedimentology*, *66*(4), 1361–1385. https://doi.org/10.1111/sed.12573

Peleg, O., Guy-Haim, T., Yeruham, E., Silverman, J., & Rilov, G. (2020). Tropicalization may invert trophic state and carbon budget of shallow temperate rocky reefs. *Journal of Ecology*, *108*(3), 844–854. https://doi.org/10.1111/1365-2745.13329

Polton, J. A., Smith, J. A., MacKinnon, J. A., & Tejada-Martínez, A. E. (2008). Rapid generation of high-frequency internal waves beneath a wind and wave forced oceanic surface mixed layer. *Geophysical Research Letters*, *35*(13), L13602. https://doi.org/10.1029/2008GL033856

Pomar, L., Baceta, J. I., Hallock, P., Mateu-Vicens, G., & Basso, D. (2017). Reef building and carbonate production modes in the west-central Tethys during the Cenozoic. *Marine and Petroleum Geology*, *83*, 261–304. https://doi.org/10.1016/j.marpetgeo.2017.03.015

Pomar, L., Morsilli, M., Hallock, P., & Bádenas, B. (2012). Internal waves, an under-explored source of turbulence events in the sedimentary record. *Earth-Science Reviews*, *111*(1–2), 56–81. https://doi.org/10.1016/j.earscirev.2011.12.005

Porat, N., Wintle, A. G., & Ritte, M. (2003). Mode and timing of kurkar and hamra formation, central coastal plain, Israel. *Israel Journal of Earth Sciences*, *53*, 13–25.

Quaresma, L. S., Vitorino, J., Oliveira, A., & da Silva, J. (2007). Evidence of sediment resuspension by nonlinear internal waves on the western Portuguese mid-shelf. *Marine Geology*, *246*(2–4), 123–143. https://doi.org/10.1016/j.margeo.2007.04.019

R Core Team. (2024). *R: A Language and Environment for Statistical Computing*. Http://Www.r-Project.Org/.

Reich, T., Ben-Ezra, T., Belkin, N., Tsemel, A., Aharonovich, D., Roth-Rosenberg, D., Givati, S., Bialik, O., Herut, B., Berman-Frank, I., Frada, M., Krom, M. D., Lehahn, Y., Rahav, E., & Daniel Sher. (2021). Seasonal dynamics of phytoplankton and bacterioplankton at the ultra-oligotrophic southeastern Mediterranean Sea. *BioRxiv*. https://doi.org/10.1101/2021.03.24.436734

Reiche, S., Hübscher, C., Brenner, S., Betzler, C., & Hall, J. K. (2018). The role of internal waves in the late Quaternary evolution of the Israeli continental slope. *Marine Geology*, *406*(September), 177–192. https://doi.org/10.1016/j.margeo.2018.09.013

Richardson, K., & Bendtsen, J. (2019). Vertical distribution of phytoplankton and primary production in relation to nutricline depth in the open ocean. *Marine Ecology Progress Series*, *620*, 33–46.

https://doi.org/10.3354/meps12960

Rilov, G. (2013). Regional extinctions and invaders' domination: an ecosystem phase-shift of Levant reef. *Rapport de La Commission Internationale Pour l'Exploration Scientifique de La Mér Méditerranée, 40*, 782–783.

Rilov, G. (2016). Multi-species collapses at the warm edge of a warming sea. *Scientific Reports*, *6*(1), 36897. https://doi.org/10.1038/srep36897

Rilov, G., & Galil, B. (2009). Marine Bioinvasions in the Mediterranean Sea – History, Distribution and Ecology. In G. Rilov & J. A. Crooks (Eds.), *Biological Invasions in Marine Ecosystems* (pp. 549–575). Springer,Ecological Studies (Analysis and Synthesis) 204. https://doi.org/10.1007/978-3-540-79236-9_31

Rilov, G., Peleg, O., Yeruham, E., Garval, T., Vichik, A., & Raveh, O. (2018). Alien turf: Overfishing, overgrazing and invader domination in south-eastern Levant reef ecosystems. *Aquatic Conservation: Marine and Freshwater Ecosystems*, *28*(2), 351–369. https://doi.org/10.1002/aqc.2862

Rocha, L. A., Pinheiro, H. T., Shepherd, B., Papastamatiou, Y. P., Luiz, O. J., Pyle, R. L., & Bongaerts, P. (2018). Mesophotic coral ecosystems are threatened and ecologically distinct from shallow water reefs. *Science*, *361*(6399), 281–284. https://doi.org/10.1126/science.aaq1614

Sade, A., Hall, J. K., Golan, A., Amit, G., Gur-Arie, L., Tibor, G., Ben-Avraham, Z., Hübscher, C., & Ben-Dor, E. (2006). *High resolution bathymetry of the Mediterranean sea off northern Israel*. GSI report GSI/20/2006, IOLR report H44/2006.

Sala, E., Kizilkaya, Z., Yildirim, D., & Ballesteros, E. (2011). Alien Marine Fishes Deplete Algal Biomass in the Eastern Mediterranean. *PLoS ONE*, *6*(2), e17356. https://doi.org/10.1371/journal.pone.0017356

Schlager, W. (2005). *Carbonate Sedimentology and Sequence Stratigraphy* (W. Schlager (ed.)). SEPM concepts in sedimentology and paleontology, volume 8. https://doi.org/10.2110/csp.05.08

Schmidt, C., Titelboim, D., Brandt, J., Herut, B., Abramovich, S., Almogi-Labin, A., & Kucera, M. (2016). Extremely heat tolerant photo-symbiosis in a shallow marine benthic foraminifera. *Scientific Reports*, *6*(1), 30930. https://doi.org/10.1038/srep30930

Sherman, C., Schmidt, W., Appeldoorn, R., Hutchinson, Y., Ruiz, H., Nemeth, M., Bejarano, I., Motta, J. J. C., & Xu, H. (2016). Sediment dynamics and their potential influence on insular-slope mesophotic coral ecosystems. *Continental Shelf Research*, *129*, 1–9. https://doi.org/10.1016/j.csr.2016.09.012

Shtienberg, G., Dix, J. K., Roskin, J., Waldmann, N., Bookman, R., Bialik, O. M., Porat, N., Taha, N., & Sivan, D. (2017). New perspectives on coastal landscape reconstruction during the Late Quaternary: A test case from central Israel. *Palaeogeography, Palaeoclimatology, Palaeoecology*, *468*. https://doi.org/10.1016/j.palaeo.2016.12.045

Silva, M., & MacDonald, I. (2017). Habitat suitability modeling for mesophotic coral in the northeastern Gulf of Mexico. *Marine Ecology Progress Series*, *583*, 121–136. https://doi.org/10.3354/meps12336

Sisma-Ventura, G., Yam, R., Kress, N., & Shemesh, A. (2016). Water column distribution of stable isotopes and carbonate properties in the {South}-eastern {Levantine} basin ({Eastern} {Mediterranean}): {Vertical} and temporal change. *Journal of Marine Systems*, *158*, 13–25. https://doi.org/https://doi.org/10.1016/j.jmarsys.2016.01.012

Sisma-Ventura, G., Yam, R., & Shemesh, A. (2014). Recent unprecedented warming and oligothrophy of the Eastern Mediterranean Sea within the last millennium. *Geophysical Research Letters*, *41*(14), 5158–5166. https://doi.org/10.1002/2014GL060393

Soulsby, R. L., & Whitehouse, R. J. (1997). January. Threshold of sediment motion in coastal environments. In *Pacific Coasts and Ports' 97: Proceedings of the 13th Australasian Coastal and Ocean Engineering Conference and the 6th Australasian Port and Harbour Conference* (pp. 145–150). Christchurch, NZ: Centre for Advanced Engineering, University of Canterbury. https://doi.org/10.3316/informit.929741720399033

Soulsby, R. L., Whitehouse, R. J. S., & Marten, K. V. (2012). Prediction of time-evolving sand ripples in shelf seas. *Continental Shelf Research*, *38*, 47–62. https://doi.org/10.1016/j.csr.2012.02.016

Stambler, N. (2014). The Mediterranean Sea – Primary Productivity. In S. Goffredo & Z. Dubinsky (Eds.), *The Mediterranean Sea* (pp. 113–121). Springer Netherlands. https://doi.org/10.1007/978-94-007-6704-1_7

Stastna, M., & Lamb, K. G. (2008). Sediment resuspension mechanisms associated with internal waves in coastal waters. *Journal of Geophysical Research*, *113*(C10), C10016. https://doi.org/10.1029/2007JC004711

Storlazzi, C. ., Ogston, A. ., Bothner, M. ., Field, M. ., & Presto, M. . (2004). Wave- and tidally-driven flow and sediment flux across a fringing coral reef: Southern Molokai, Hawaii. *Continental Shelf Research*, *24*(12), 1397–1419. https://doi.org/10.1016/j.csr.2004.02.010

Stow, D. A. V., Hernández-Molina, F. J., Llave, E., Sayago-Gil, M., Díaz del Río, V., & Branson, A. (2009). Bedform-velocity matrix: The estimation of bottom current velocity from bedform observations. *Geology*, *37*(4), 327–330. https://doi.org/10.1130/G25259A.1

Studivan, M. S., & Voss, J. D. (2018). Population connectivity among shallow and mesophotic Montastraea cavernosa corals in the Gulf of Mexico identifies potential for refugia. *Coral Reefs*, *37*(4), 1183–1196. https://doi.org/10.1007/s00338-018-1733-7

Talley, L. D., Pickard, G. L., Emery, W. J., & Swift, J. H. (2011). *Descriptive Physical Oceanography: An Introduction* (6th ed.). Elsevier - Academic Press.

Thingstad, T. F., Krom, M. D., Mantoura, R. F. C., Flaten, G. A. F., Groom, S., Herut, B., Kress, N., Law, C. S., Pasternak, A., Pitta, P., Psarra, S., Rassoulzadegan, F., Tanaka, T., Tselepides, A., Wassmann, P., Woodward, E. M. S., Riser, C. W., Zodiatis, G., & Zohary, T. (2005). Nature of Phosphorus Limitation in the Ultraoligotrophic Eastern Mediterranean. *Science*, *309*(5737), 1068–1071. https://doi.org/10.1126/science.1112632

Valle-Levinson, A., Kourafalou, V. H., Smith, R. H., & Androulidakis, Y. (2020). Flow structures over mesophotic coral ecosystems in the eastern Gulf of Mexico. *Continental Shelf Research*, *207*, 104219. https://doi.org/10.1016/j.csr.2020.104219

van Haren, H. (2017). Internal Waves and Bedforms. In J. Guillén, J. Acosta, F. Chiocci, & A. Palanques (Eds.), *Atlas of Bedforms in the Western Mediterranean* (pp. 25–28). Springer International Publishing. https://doi.org/10.1007/978-3-319-33940-5_5

Varzi, A. G., Fallati, L., Savini, A., Bracchi, V. A., Bazzicalupo, P., Rosso, A., Sanfilippo, R., Bertolino, M., Muzzupappa, M., & Basso, D. (2023). Geomorphology of coralligenous reefs offshore southeastern Sicily (Ionian Sea). *Journal of Maps*, 1–13. https://doi.org/10.1080/17445647.2022.2161963

Vasilief, I. (2010). *QtiPlot - Data Analysis and Scientific Visualisation*. http://soft.proindependent.com/qtiplot.html

Wall, M., Schmidt, G. M., Janjang, P., Khokiattiwong, S., & Richter, C. (2012). Differential Impact of

Monsoon and Large Amplitude Internal Waves on Coral Reef Development in the Andaman Sea. *PLoS ONE*, *7*(11), e50207. https://doi.org/10.1371/journal.pone.0050207

Wang, Y.-H., Dai, C.-F., & Chen, Y.-Y. (2007). Physical and ecological processes of internal waves on an isolated reef ecosystem in the South China Sea. *Geophysical Research Letters*, *34*(18), L18609. https://doi.org/10.1029/2007GL030658

Wentworth, C. K. (1922). A Scale of Grade and Class Terms for Clastic Sediments. *The Journal of Geology*, *30*(5), 377–392. https://doi.org/10.1086/622910

Wickham, H. (2009). *ggplot2*. Springer New York. https://doi.org/10.1007/978-0-387-98141-3

Wilckens, H., Schwenk, T., Lüdmann, T., Betzler, C., Zhang, W., Chen, J., Hernández-Molina, F. J., Lefebvre, A., Cattaneo, A., Spieß, V., & Miramontes, E. (2023). Factors controlling the morphology and internal sediment architecture of moats and their associated contourite drifts. *Sedimentology*, *70*(5), 1472–1495. https://doi.org/10.1111/sed.13093

Williams, D. M., Wolanski, E., & Andrews, J. C. (1984). Transport mechanisms and the potential movement of planktonic larvae in the central region of the Great Barrier Reef. *Coral Reefs*, *3*(4), 229–236. https://doi.org/10.1007/BF00288259

Wolanski, E., & Delesalle, B. (1995). Upwelling by internal waves, Tahiti, French Polynesia. *Continental Shelf Research*, *15*(2–3), 357–368. https://doi.org/10.1016/0278-4343(93)E0004-R

Wyatt, A. S. J., Leichter, J. J., Toth, L. T., Miyajima, T., Aronson, R. B., & Nagata, T. (2020). Heat accumulation on coral reefs mitigated by internal waves. *Nature Geoscience*, *13*(1), 28–34. https://doi.org/10.1038/s41561-019-0486-4

Wynn, R. B., & Stow, D. A. V. (2002). Classification and characterisation of deep-water sediment waves. *Marine Geology*, *192*(1–3), 7–22. https://doi.org/10.1016/S0025-3227(02)00547-9

Yahel, R., Yahel, G., & Genin, A. (2002). Daily cycles of suspended sand at coral reefs: A biological control. *Limnology and Oceanography*, *47*(4), 1071–1083. https://doi.org/10.4319/lo.2002.47.4.1071